The Astronomical Journal, 162:87 (15pp), 2021 September https://doi.org/10.3847/1538-3881/ac0432


# TOI-1231 b: A Temperate, Neptune-sized Planet Transiting the Nearby M3 Dwarf NLTT 24399

Jennifer A. Burt[1], Diana Dragomir[2], Paul Mollière[3], Allison Youngblood[4], Antonio García Muñoz[5], John McCann[6], Laura Kreidberg[3], Chelsea X. Huang[7,45], Karen A. Collins[8], Jason D. Eastman[8], Lyu Abe[9], Jose M. Almenara[10], Ian J. M. Crossfield[11], Carl Ziegler[12], Joseph E. Rodriguez[13], Eric E. Mamajek[1], Keivan G. Stassun[14,15], Samuel P. Halverson[1], Steven Villanueva, Jr.[7,46], R. Paul Butler[16], Sharon Xuesong Wang[17,18], Richard P. Schwarz[19], George R. Ricker[7], Roland Vanderspek[7], David W. Latham[8], S. Seager[7,20,21], Joshua N. Winn[64], Jon M. Jenkins[23], Abdelkrim Agabi[9], Xavier Bonfils[10], David Ciardi[24], Marion Cointepas[10,25], Jeffrey D. Crane[17], Nicolas Crouzet[26], Georgina Dransfield[27], Fabo Feng[28,29], Elise Furlan[24], Tristan Guillot[9], Arvind F. Gupta[30,31], Steve B. Howell[23], Eric L. N. Jensen[32], Nicholas Law[33], Andrew W. Mann[33], Wenceslas Marie-Sainte[34], Rachel A. Matson[35], Elisabeth C. Matthews[25], Djamel Mékarnia[9], Joshua Pepper[36], Nic Scott[23], Stephen A. Shectman[17], Joshua E. Schlieder[37], François-Xavier Schmider[9], Daniel J. Stevens[38,39,47], Johanna K. Teske[16], Amaury H. M. J. Triaud[27], David Charbonneau[8], Zachory K. Berta-Thompson[40], Christopher J. Burke[7], Tansu Daylan[7,48], Thomas Barclay[41,42], Bill Wohler[23,43], and C. E. Brasseur[44]

[1] Jet Propulsion Laboratory, California Institute of Technology, 4800 Oak Grove Drive, Pasadena, CA 91109, USA
[2] Department of Physics and Astronomy, University of New Mexico, 1919 Lomas Blvd NE, Albuquerque, NM 87131, USA
[3] Max-Planck-Institut für Astronomie, Königstuhl 17, D-69117, Heidelberg, Germany
[4] Laboratory for Atmospheric and Space Physics, 1234 Innovation Drive, Boulder, CO, 80303, USA
[5] AIM, CEA, CNRS, Université Paris-Saclay, Université de Paris, Gif-sur-Yvette, France
[6] Department of Physics, University of California, Santa Barbara, CA 93106, USA
[7] Department of Physics and Kavli Institute for Astrophysics and Space Research, Massachusetts Institute of Technology, Cambridge, MA 02139, USA
[8] Center for Astrophysics |Harvard & Smithsonian, 60 Garden Street, Cambridge, MA 02138, USA
[9] Université Côte d'Azur, Observatoire de la Côte d'Azur, CNRS, Laboratoire Lagrange, Bd de l'Observatoire, CS 34229, F-06304 Nice cedex 4, France
[10] Univ. Grenoble Alpes, CNRS, IPAG, F-38000, Grenoble, France
[11] Physics & Astronomy Department, University of Kansas, Lawrence, KS, USA
[12] Dunlap Institute for Astronomy and Astrophysics, University of Toronto, 50 St. George Street, Toronto, Ontario M5S 3H4, Canada
[13] Department of Physics and Astronomy, Michigan State University, East Lansing, MI, 48824 USA
[14] Department of Physics and Astronomy, Vanderbilt University, Nashville, TN 37235, USA
[15] Department of Physics, Fisk University, Nashville, TN 37208, USA
[16] Earth & Planets Laboratory, Carnegie Institution for Science, 5241 Broad Branch Road, NW, Washington, DC 20015, USA
[17] The Observatories of the Carnegie Institution for Science, 813 Santa Barbara Street, Pasadena, CA 91101, USA
[18] Department of Astronomy, Tsinghua University, Beijing 100084, People's Republic of China
[19] Patashnick Voorheesville Observatory, Voorheesville, NY 12186, USA
[20] Department of Earth, Atmospheric and Planetary Sciences, Massachusetts Institute of Technology, Cambridge, MA 02139, USA
[21] Department of Aeronautics and Astronautics, MIT, 77 Massachusetts Avenue, Cambridge, MA 02139, USA
[22] Department of Astrophysical Sciences, Princeton University, 4 Ivy Lane, Princeton, NJ 08544, USA
[23] NASA Ames Research Center, Moffett Field, CA 94035, USA
[24] NASA Exoplanet Science Institute, Infrared Processing & Analysis Center, Jet Propulsion Laboratory, California Institute of Technology, Pasadena CA 91125, USA
[25] Observatoire de l'Université de Genéve, Chemin des Maillettes 51, 1290 Versoix, Switzerland
[26] European Space Agency (ESA), European Space Research and Technology Centre (ESTEC), Keplerlaan 1, 2201 AZ Noordwijk, The Netherlands
[27] School of Physics & Astronomy, University of Birmingham, Edgbaston, Birmingham, B15 2TT, UK
[28] Tsung-Dao Lee Institute, Shanghai Jiao Tong University, 800 Dongchuan Road, Shanghai 200240, People's Republic of China
[29] Department of Astronomy, School of Physics and Astronomy, Shanghai Jiao Tong University, 800 Dongchuan Road, Shanghai 200240, People's Republic of China
[30] Department of Astronomy & Astrophysics, 525 Davey Laboratory, The Pennsylvania State University, University Park, PA, 16802, USA
[31] Center for Exoplanets and Habitable Worlds, 525 Davey Laboratory, The Pennsylvania State University, University Park, PA, 16802, USA
[32] Dept. of Physics & Astronomy, Swarthmore College, Swarthmore PA 19081, USA
[33] Department of Physics and Astronomy, The University of North Carolina at Chapel Hill, Chapel Hill, NC 27599-3255, USA
[34] Concordia Station, IPEV/PNRA, Antarctica
[35] U.S. Naval Observatory, Washington, DC 20392, USA
[36] Department of Physics, Lehigh University, 16 Memorial Drive East, Bethlehem, PA 18015, USA
[37] Exoplanets and Stellar Astrophysics Laboratory, Code 667, NASA Goddard Space Flight Center, Greenbelt, MD, 20771, USA
[38] Department of Astronomy & Astrophysics, The Pennsylvania State University, 525 Davey Lab, University Park, PA 16802, USA
[39] Center for Exoplanets and Habitable Worlds, The Pennsylvania State University, 525 Davey Lab, University Park, PA 16802, USA
[40] University of Colorado Boulder, Boulder, CO 80309, USA
[41] NASA Goddard Space Flight Center, 8800 Greenbelt Road, Greenbelt, MD 20771, USA
[42] University of Maryland, Baltimore County, 1000 Hilltop Circle, Baltimore, MD 21250, USA
[43] SETI Institute, Mountain View, CA 94043, USA
[44] Space Telescope Science Institute, 3700 San Martin Drive, Baltimore, MD 21218, USA
*Received 2020 November 18; revised 2021 May 13; accepted 2021 May 20; published 2021 August 3*

[45] Juan Carlos Torres Fellow.
[46] Pappalardo Fellow.
[47] Eberly Research Fellow.
[48] Kavli Fellow.

## Abstract

We report the discovery of a transiting, temperate, Neptune-sized exoplanet orbiting the nearby ($d = 27.5$ pc), M3V star TOI-1231 (NLTT 24399, L 248-27, 2MASS J10265947-5228099). The planet was detected using photometric data from the Transiting Exoplanet Survey Satellite and followed up with observations from the Las Cumbres Observatory and the Antarctica Search for Transiting ExoPlanets program. Combining the photometric data sets, we find that the newly discovered planet has a radius of $3.65^{+0.16}_{-0.15}\,R_{\oplus}$ and an orbital period of 24.246 days. Radial velocity measurements obtained with the Planet Finder Spectrograph on the Magellan Clay telescope confirm the existence of the planet and lead to a mass measurement of $15.5 \pm 3.3\,M_{\oplus}$. With an equilibrium temperature of just 330 K, TOI-1231 b is one of the coolest small planets accessible for atmospheric studies thus far, and its host star's bright near-infrared brightness ($J = 8.88$, $K_s = 8.07$) makes it an exciting target for the *Hubble Space Telescope* and the *James Webb Space Telescope*. Future atmospheric observations would enable the first comparative planetology efforts in the 250–350 K temperature regime via comparisons with K2-18 b. Furthermore, TOI-1231's high systemic radial velocity (70.5 km s$^{-1}$) may allow for the detection of low-velocity hydrogen atoms escaping the planet by Doppler, shifting the H I Ly$\alpha$ stellar emission away from the geocoronal and interstellar medium absorption features.


*Unified Astronomy Thesaurus concepts:* Exoplanet astronomy (486); Transit photometry (1709); Radial velocity (1332); Mini Neptunes (1063)

## 1. Introduction

The observing strategy adopted by NASA's Transiting Exoplanet Survey Satellite (TESS; Ricker et al. 2014), wherein each hemisphere is divided into 13 sectors, each of which is surveyed for roughly 28 days, is producing the most comprehensive all-sky search for transiting planets. This approach has already proven its capability to detect both large and small planets (Dragomir et al. 2019; Luque et al. 2019; Rodriguez et al. 2019; Wang et al. 2019; Burt et al. 2020) around stars ranging from Sun-like (Huang et al. 2018) down to low-mass M dwarf stars (Vanderspek et al. 2019).

Although it enables the detection of exoplanets across the sky, TESS's survey strategy also produces significant observational biases based on orbital period. Exoplanets must transit their host stars at least twice within TESS's observing span in order to be detected with the correct period by the Science Processing Operations Center (SPOC) pipeline, which searches the 2-minute cadence TESS data obtained for preselected target stars (Jenkins et al. 2016). Because 74% of TESS's total sky coverage is observed only for $\leqslant$28 days, the majority of TESS exoplanets detected by the SPOC are expected to have periods less than 14 days. Simulations of the TESS exoplanet yield presented in Sullivan et al. (2015) find mean and median orbital periods of 13.48 and 8.19 days, respectively, among all detected planets. Similarly, Barclay et al. (2018) found mean and median periods of 10.23 and 7.03 days among the full set of detected planets, and those values drop to just 7.42 and 5.89 days when considering the stars only observed during a single TESS sector. And additional simulations from Jiang et al. (2019) show that for stars observed only in a single sector, the expected mean value of the most frequently detected orbital period is 5.01 days, with a most detected range of 2.12–11.82 days. Even when considering the ecliptic poles, where TESS carries out 351 days of observing coverage during its primary mission, the expected mean orbital period is still only 10.93 days, with a most detected range from 3.35 to 35.65 days.

Of the 1994 TESS objects of interest (TOIs) identified as planet candidates using Sectors 1–26 of the primary mission, only ~14% have periods longer than 14 days.[49] But these longer period (and thereby cooler) candidates are some of the most intriguing targets for atmospheric characterization. This is especially true for Neptune-sized planets, whose lower temperatures could spark several marked changes in the expected atmospheric chemistry: disequilibrium due to rain out is relevant, water clouds may form, and ammonia is the dominant carrier of nitrogen (see, e.g., Morley et al. 2014). Thus these cooler TOIs merit additional attention and focused follow-up efforts both to confirm their planetary nature and to obtain the precise mass measurements necessary for correct interpretation of future transmission spectroscopy observations (Batalha et al. 2019).

Here we report the discovery of a Neptune-sized planet transiting TOI-1231 (NLTT 24399, L 248-27, TIC 447061717, 2MASS J10265947-5228099), a $V = 12.3$ mag M3V star (Gaidos et al. 2014) in the Vela constellation at $d = 27.493 \pm 0.0123$ pc ($\varpi = 36.3726 \pm 0.0163$ mas; Gaia EDR3 van Leeuwen et al. 2021). This paper is organized as follows. In Section 2 we characterize the host star using details from published catalogs and new data obtained once the TESS planet candidate was identified. In Section 3 we describe the initial discovery of TOI-1231 b and the follow-up data obtained in an effort to characterize the planet. In Section 4 we outline the procedure used to perform a joint fit to the host star and planet, and then in Section 5 we conclude with a discussion of the planet's promising potential for future atmospheric characterization.

## 2. Stellar Data and Characterization

### 2.1. Background

TOI-1231 was first reported as a high proper motion star (0.″35 yr$^{-1}$) by Luyten (1957, as LTT 3840 and L 248-27), and later in the Revised NLTT catalog (Luyten 1979, as NLTT 24399). Over the past decade, the star has appeared in several surveys of high proper motion Two Micron All Sky Survey (2MASS) and *Wide-field Infrared Survey Explorer* (*WISE*) stars and nearby M dwarfs (e.g., Lépine & Gaidos 2011; Frith et al. 2013; Kirkpatrick et al. 2014; Schneider et al. 2016). The only previous spectral characterization of TOI-1231 was by Gaidos et al. (2014) in the CONCH-SHELL survey, who reported a spectral type of M3V. Previous estimates of the basic stellar parameters were reported by Gaidos et al. (2014), Muirhead et al. (2018), and Stassun et al. (2019).

### 2.2. Astrometry and Photometry

Stellar astrometry and visible and infrared photometry are compiled in Table 1. The positions, proper motions, parallax,

[49] https://tev.mit.edu/data/collection/193/

**Table 1**
Astrometry and Photometry for TOI-1231

| Parameter | Value | Source |
|---|---|---|
| Designations | TIC 447061717 | Stassun et al. (2019) |
| | NLTT 24399 | Luyten (1979) |
| R.A. (ICRS, J2000) | **10:26:59.34** | Gaia **EDR3** |
| decl. (ICRS, J2000) | **−52 28 04.16** | Gaia **EDR3** |
| $\mu$ R.A. (mas yr$^{-1}$) | **−89.394 ± 0.019** | Gaia **EDR3** |
| $\mu$ decl. (mas yr$^{-1}$) | **361.546 ± 0.015** | Gaia **EDR3** |
| Parallax (mas) | **36.3726 ± 0.0163** | Gaia **EDR3**[a] |
| Distance (pc) | **27.4932 ± 0.0123** | Gaia **EDR3**[a] |
| $v_R$ (km s$^{-1}$) | 70.48 ± 0.54 | Gaia DR2 |
| SpT | M3V | Gaidos et al. (2014) |
| $B$ | 13.739 ± 0.028 | APASS/DR10 |
| $V$ | 12.322 ± 0.023 | APASS/DR10 |
| $g'$ | 12.997 ± 0.044 | APASS/DR10 |
| $r'$ | 11.806 ± 0.070 | APASS/DR10 |
| $i'$ | 10.754 ± 0.175 | APASS/DR10 |
| TESS | 10.2565 ± 0.007 | TIC8 |
| $G$ | **11.3612 ± 0.0009** | Gaia **EDR3** |
| $G_{BP}$ | **12.5440 ± 0.0022** | Gaia **EDR3** |
| $G_{RP}$ | **10.2735 ± 0.0015** | Gaia **EDR3** |
| $J$ | 8.876 ± 0.027 | 2MASS |
| $H$ | 8.285 ± 0.038 | 2MASS |
| $K_s$ | 8.069 ± 0.026 | 2MASS |
| $W_1$ | 7.922 ± 0.024 | *WISE* |
| $W_2$ | 7.826 ± 0.020 | *WISE* |
| $W_3$ | 7.732 ± 0.017 | *WISE* |
| $W_4$ | 7.515 ± 0.091 | *WISE* |
| $U$ (km s$^{-1}$) | −20.25 ± 0.24 | This work |
| $V$ (km s$^{-1}$) | −73.37 ± 0.36 | This work |
| $W$ (km s$^{-1}$) | 39.45 ± 0.33 | This work |
| $S_{tot}$(km s$^{-1}$) | 85.73 ± 0.35 | This work |

**Note.**
[a]:Correction of −17 $\mu$as applied to the Gaia parallax following the prescription in Lindegren et al. (2021).

and Gaia photometry are from Gaia EDR3 (van Leeuwen et al. 2021), whereas the radial velocity is from Gaia DR2 (Gaia Collaboration et al. 2018). We convert the astrometry to Galactic velocities following ESA (1997).[50] Photometry is reported from AAVSO Photometric All-Sky Survey (APASS) Data Release 10 (Henden et al. 2016),[51] the TESS Input Catalog (TIC8), 2MASS (Cutri et al. 2003), and *WISE* (Cutri et al. 2012).

### 2.3. Spectral Energy Distribution

We analyzed TOI-1231's broadband spectral energy distribution (SED) alongside its Gaia EDR3 parallax to determine an empirical measurement of the star's radius, following Stassun & Torres (2016) and Stassun et al. (2017, 2018). Together, the available photometry described here and listed in Table 1 cover the full stellar SED from 0.4 to 22 $\mu$m (see Figure 1). We exclude the APASS/**DR10** data from the SED fit in favor of the Gaia EDR3 passbands, which cover the same wavelength range and have smaller errors, but note that we adopt an error floor of 0.03 mag on the photometry because the systematics on the absolute flux calibration between photometric systems is 2%–3%.

We performed the fit using NextGen stellar atmosphere models, placing a prior on the star's surface gravity ($\log g$) from the TESS Input Catalog (TIC8). We set the stellar effective temperature equal to the result from the Cool Dwarf Catalog ($T_{\rm eff} = 3557 \pm 82$ K, Muirhead et al. 2018) and the extinction to zero due to the star's proximity (within the Local Bubble), which is consistent with the reddening value of $E_{B-V} = 0.001 \pm 0.015$ from Lallement et al. (2018).[52] The resulting SED fit is quite good (Figure 1, top) with a reduced $\chi^2$ of 1.9. The best-fit stellar metallicity is [Fe/H] = 0.0 ± 0.3. Integrating the model SED results in the bolometric flux at Earth being $F_{\rm bol} = (1.345 \pm 0.047) \times 10^{-9}$ erg s$^{-1}$ cm$^{-2}$ ($m_{\rm bol} = 10.682 \pm 0.032$ on IAU 2015 bolometric magnitude scale).[53] Taking the $F_{\rm bol}$ and $T_{\rm eff}$ together with the Gaia EDR3 parallax gives the stellar radius as $R_\star = 0.466 \pm 0.021\ R_\odot$ and the stellar mass as $M_\star = 0.485 \pm 0.024\ M_\odot$ based on the empirical $M_{Ks}$ versus mass relations from Mann et al. (2019).[54]

#### 2.3.1. Speckle Observations

High-angular resolution imaging is needed to search for nearby sources that can contaminate the TESS photometry, resulting in a diluted transit and an underestimated planetary radius, and also to search for faint stars that might be responsible for the transit signal. We searched for nearby sources to TOI-1231 with SOAR speckle imaging (Tokovinin et al. 2018) on UT 2019 December 12 in *I*-band, a similar near-IR bandpass as used by TESS. Further details of observations from the SOAR TESS survey are available in Ziegler et al. (2020). We detected no nearby stars within 3″ of TOI-1231 within the 5$\sigma$ detection sensitivity limits of the observation, which are plotted along with the speckle autocorrelation function in the middle panel of Figure 1. Using the measured detection sensitivity from the SOAR observation and the estimated $T_{\rm eff}$ of the target star along with main-sequence stellar SEDs (Kraus & Hillenbrand 2012), we can effectively rule out a main-sequence companion within angular resolutions between 0.″2 and 3.″0 or projected physical separations of 5.5–83 au.

Speckle interferometric images of TOI-1231 were also obtained on UT 2020 March 13 using the Zorro[55] instrument mounted on Gemini-South. Zorro observes simultaneously in two bands (832 ± 40 nm and 562 ± 54 nm) obtaining diffraction limited images with inner working angles of 0.026 and 0.017 arcseconds, respectively. The TOI-1231 data set consisted of 5 minutes of total integration time taken as sets of 1000 × 0.06 s images. All of the images were combined using Fourier analysis techniques, examined for stellar companions, and used to produce reconstructed speckle images

[50] $U$ toward Galactic center, $V$ in direction of Galactic spin, and $W$ toward north Galactic pole (ESA 1997).
[51] https://www.aavso.org/apass
[52] STILISM: https://stilism.obspm.fr/
[53] Besides this analysis, we also estimate $m_{\rm bol}$ via other methods. Applying the M dwarf bolometric magnitude relations of Casagrande et al. (2008) with the 2MASS JHK$_s$ photometry, we estimate $m_{\rm bol} = 10.74 \pm 0.02$. Using the $V - J$ versus $BC_{Ks}$ relation from Mann et al. (2015) applied to the 2MASS $K_s$ magnitude, we estimate $m_{\rm bol} = 10.79$. Fitting BT-Settl-CIFIST synthetic spectra to the photometry in Table 1 using the virtual observatory SED analyzer (VOSA) SED Analyzer (Bayo et al. 2008) yielded $F_{\rm bol} = (1.363 \pm 0.116) \times 10^{-9}$ erg s$^{-1}$ cm$^{-2}$ ($m_{\rm bol} = 10.666 \pm 0.095$) for $T_{\rm eff} = 3600$ K, $\log g = 4.5$, [M/H] = 0. These values provide independent checks, but we adopt the $F_{\rm bol}$ and $m_{\rm bol}$ in the text.
[54] For $M_{Ks} = 5.861 \pm 0.026$ and assuming [Fe/H] = 0.
[55] https://www.gemini.edu/sciops/instruments/alopeke-zorro/

(see Howell et al. 2011). The speckle imaging results reveal TOI-1231 to be a single star to contrast limits of ∼5 to 8 magnitudes, eliminating the possibility of any main-sequence companions to TOI-1231 ($d = 27.6$ pc) within the spatial limits of 3–33 au (Figure 1, bottom).

### 2.4. Stellar Kinematics and Population

Using the astrometry and radial velocity data from Gaia Collaboration et al. (2018), we calculate the heliocentric Galactic velocity for TOI-1231 to be $(U, V, W) = (-20.25, -73.37, 39.45 \pm 0.24, 0.36, 0.33)$ km s$^{-1}$, with total velocity $S_{\rm tot} = 85.73 \pm 0.35$ km s$^{-1}$. Compared with the local standard of rest (LSR) of Schönrich et al. (2010), we estimate velocities of $(U, V, W) = (-10.2, -62.4, 46.5)$ km s$^{-1}$, with $S_{LSR} = 78.4$ km s$^{-1}$. We use the BANYAN Σ (Bayesian Analysis for Nearby Young AssociatioNs Σ; Gagné et al. 2018) tool to estimate membership probabilities to nearby young associations within 150 pc; however, the probabilities are ≪0.1% for any of the known nearby stellar groups (all with ages <1 Gyr), and the star is classified as "*field*." Following Bensby et al. (2014), we use the Galactic velocity to estimate kinematic membership probabilities to the Milky Way's principal populations, using a 4-population model for the thin disk, thick disk, halo, and Hercules stream.[56] We estimate kinematic membership probabilities of $P$(thin) = 16.7%, $P$(thick) = 64.5%, $P$(Hercules) = 18.7%, and $P$(halo) = 0.06%. However, the star's LSR velocity places it among the Hercules stream member in Figure 29 of Bensby et al. (2014). Mackereth & Bovy (2018) calculated parameters of the star's Galactic orbit using Stäckel approximation with the Gaia Collaboration et al. (2018) astrometry, and found an eccentricity of 0.332, $z_{\rm max} = 0.905$ kpc, a perigalacticon of $r_{\rm peri} = 4.02$ kpc, and an apogalacticon of $r_{\rm ap} = 8.03$ kpc,[57] i.e., we are catching the star near its apogalacticon.

We also searched for companions of TOI-1231 in the Gaia Collaboration et al. (2018) catalog via the 50 pc sample of Torres et al. (2019). Given the mass of 0.46 $M_\odot$, we estimate the tidal radius for TOI-1231 (where bound companions would likely be found) to be 1.04 pc (Mamajek et al. 2013), which corresponds to a projected radius of ∼2.°2. Querying the Torres et al. (2019) catalog for stars with proper motions and parallaxes within 20% of that of the star within 2 tidal radii (4.°4) yielded no candidate companion. Therefore, we conclude TOI-1231 to be a single star.

### 2.5. Metallicity

The $V - K_s$ versus absolute magnitude position of an M dwarf can be used to infer a photometric metallicity estimate (e.g., Johnson & Apps 2009). TOI-1231's combination of $V - K_s$ color (4.25) and absolute magnitude ($M_{Ks} = 5.86$) are consistent with it being 0.17 mag brighter than the locus for nearby M dwarfs, which Schlaufman & Laughlin (2010) estimate represents an isometallicity trend of [Fe/H] = −0.14. Using the calibrations of Johnson & Apps (2009) and Schlaufman & Laughlin (2010), this offset is consistent with a predicted metallicity of [Fe/H] = +0.05 and −0.03, respectively, i.e., approximately solar.

Gaia DR2 (Gaia Collaboration et al. 2018) has an estimate of [Fe/H] = −1.5, but for an unrealistic giant-like surface gravity

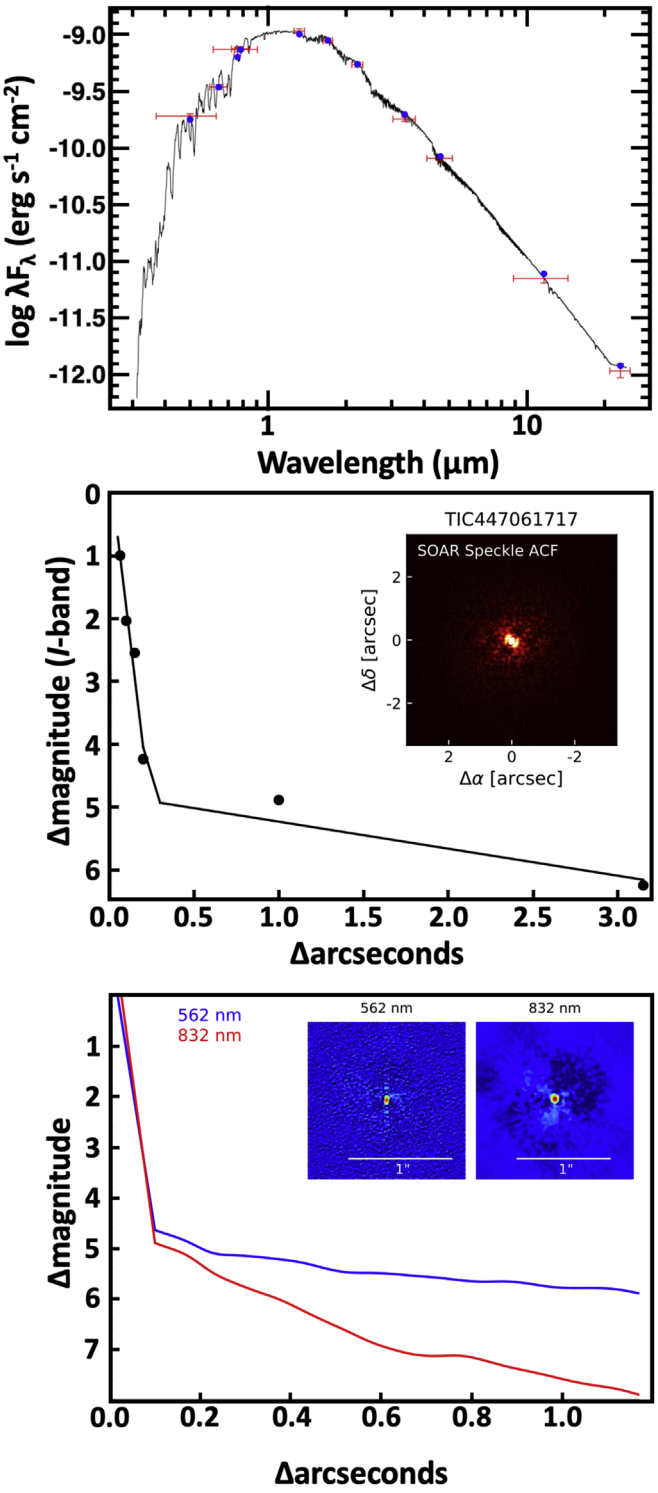


**Figure 1.** *Top*: Best-fit SED for TOI-1231. The red symbols are the observed photometric measurements and the horizontal lines show the effective width of each filter. The blue symbols depict the model flux values from the best-fit NextGen atmosphere model, which is shown in black. *Middle*: Southern Astrophysical Research telescope (SOAR) contrast curve and image (inset) for *I*-band speckle observations of TOI-1231. *Bottom*: Zorro contrast curves and images (inset) for 562 nm and 832 nm speckle observations of TOI-1231. No visual companions are detected in the field of view of either SOAR or Zorro.

[56] The Hercules stream stars contain a mix of α-enhanced old stars and younger, less α-enhanced around the solar [Fe/H] (e.g., Bensby et al. 2014), likely from the inner part of the Galaxy and kinematically heated by the Galactic bar (Dehnen 2000) and halo, although the exact type of resonant interaction responsible for the stream is still controversial (Monari et al. 2019).

[57] $R_O = 8$ kpc is assumed.

of $\log g = 3.0$ and hot $T_{\rm eff}$ of 4000 K. Taken at face value, the Gaia DR2 metallicity would predict that the star's $V - K_s$ versus $M_{Ks}$ position should be more than a magnitude below the main sequence (extrapolating the metallicity versus $\Delta M_{Ks}$ relations of Schlaufman & Laughlin 2010), well below where it is observed (~0.2 mag above the MS).

Anders et al. (2019) uses the *StarHorse* code to fit $G_B$, $G$, $G_R$, $J$, $H$, $Ks$, $W1$, and $W2$ photometry to solve for a photometric metallicity estimate consistent with $[{\rm Fe/H}] = 0.095^{+0.028}_{-0.061}$.

Taking the mean of our independent photometric metallicity estimates and that of Anders et al. (2019), we adopt a metallicity of $[{\rm Fe/H}] = +0.05 \pm 0.08$.

## 3. Exoplanet Detection and Follow-up

### 3.1. TESS Time Series Photometry

TOI-1231 was selected for transit detection observations by TESS from two input lists. It was included in the exoplanet candidate target list (CTL) that accompanied version 8 of the TESS Input Catalog (TIC; Stassun et al. 2019), and also in the Cool Dwarf Catalog (Muirhead et al. 2018). Its CTL observing priority was 0.00734, placing it among the top 3% of targets selected for transit detection by the mission, due to its brightness and small estimated stellar radius (see Sections 3.1 and 3.3 of Stassun et al. (2019) for details on the prioritization process). It was also selected for observations by TESS Guest Investigator proposal GO11180 (C. Dressing). TOI-1231 was observed by TESS from UT 2019 February 28 through 2019 March 26 as part of the Sector 9 campaign and again from UT 2019 March 26 through 2019 April 22 as part of Sector 10. The star fell on Camera 3 in both sectors, but shifted from CCD 1 in Sector 9 to CCD 2 in Sector 10.

The SPOC data for TOI-1231 can be accessed at the Mikulski Archive for Space Telescopes (MAST) website,[58] and includes both the simple aperture photometry (SAP) flux measurements (Twicken et al. 2010; Morris et al. 2017) and the presearch data conditioned simple aperture photometry (PDCSAP) flux measurements (Smith et al. 2012; Stumpe et al. 2012, 2014). These data products differ in that the instrumental variations present in the SAP measurements are removed from the PDCSAP data. The main variations are due to thermal effects and strong scattered light present at the start of each orbit, which affect the systematic error removal in PDC (see TESS data release notes[59] DRN16 and DRN17). We therefore use the quality flags provided by SPOC to mask out unreliable segments of the time series before executing the global fitting process in Section 4. We further detrend the TESS data by separating the individual spacecraft orbits (two in each sector) and fitting each orbit's flux measurements with a low order spline in order to mitigate residual trends in the photometry (Figure 2).

#### 3.1.1. TESS Transit Detection

TOI-1231 b transited once in each of Sectors 9 and 10. It was first identified as a planet candidate 5 months prior to becoming a TOI, by the TESS Single Transit Planet Candidate Working Group (TSTPC WG). The TSTPC WG focuses on searching light curves produced by the MIT Quick Look Pipeline (QLP) for single transit events, and validating and/or confirming those that are true planets, with the aim of increasing the yield of intermediate-to-long-period planets found by TESS (Villanueva et al. 2019, S. Villanueva et al. 2021 in preparation).

The two transits of TOI-1231 b were later also detected by both the MIT QLP, which searches for evidence of planet candidates in the TESS 30-minute-cadence Full Frame Images, and the SPOC pipeline, which analyzes the 2-minute cadence data that TESS obtains for preselected target stars (Jenkins et al. 2016). The TESS transits, one of which occurs in Sector 9 and the other in Sector 10, have a measured depth of 6453 ppm, a duration of 3.26 hours, and a measured period of 24.246 days.

While the depth and flat-bottomed shape of the TOI-1231 transits were suggestive of the transit signal being planetary in nature, there are a variety of false positives that can mimic this combination. The main source of false positives in the TESS Objects of Interest (TOIs) are eclipsing binaries, either as two transiting stars on grazing orbits or in the case of a background blend, which reduces the amplitude of a foreground eclipsing binary signal, causing it to be fallaciously small (e.g., Cameron 2012). The TESS vetting process is designed to guard against these false positives, and so we inspected the star's data validation report (DVR, Twicken et al. 2018; Li et al. 2019), which is based upon the SPOC 2-minute cadence data. The multisector DVR shows no signs of secondary eclipses, odd/even transit depth inconsistencies, or correlations between the depth of the transit and the size of the aperture used to extract the light curve, any of which would indicate that the transit signal originated from a nearby eclipsing binary. The DVR also showed that the location of the transit source is consistent with the position of the target star. Upon passing these vetting checks, the transit signal was assigned the identifier TOI-1231.01 and announced on the MIT TESS data alerts website[60] (Guerrero et al. 2021).

### 3.2. Ground-based Time Series Photometry

We acquired ground-based time series follow-up photometry of TOI-1231 during the times of transit predicted by the TESS data. We used the `TESS Transit Finder`, which is a customized version of the `Tapir` software package (Jensen 2013), to schedule our transit observations.

#### 3.2.1. LCO 1 m Observations

Two partial transits of TOI-1231 b were observed using the Las Cumbres Observatory Global Telescope (LCOGT) 1 m network (Brown et al. 2013) in the Pan-STARSS $z$ band on UTC 2020 January 16 by the LCOGT node at Cerro Tololo Inter-American Observatory and 2020 May 6 by the LCOGT node at Siding Spring Observatory (Figure 5, second panel). The telescopes are equipped with $4096 \times 4096$ LCO SINISTRO cameras having an image scale of $0\farcs389\,{\rm pixel}^{-1}$, resulting in a $26' \times 26'$ field of view. The images were calibrated by the standard LCOGT BANZAI pipeline and the photometric data were extracted using the `AstroImageJ` (`AIJ`) software package (Collins et al. 2017). Circular apertures with radius 12 pixels ($4\farcs7$) were used to extract the differential photometry.

[58] https://mast.stsci.edu
[59] https://archive.stsci.edu/tess/tess_drn.html
[60] http://tess.mit.edu/alerts

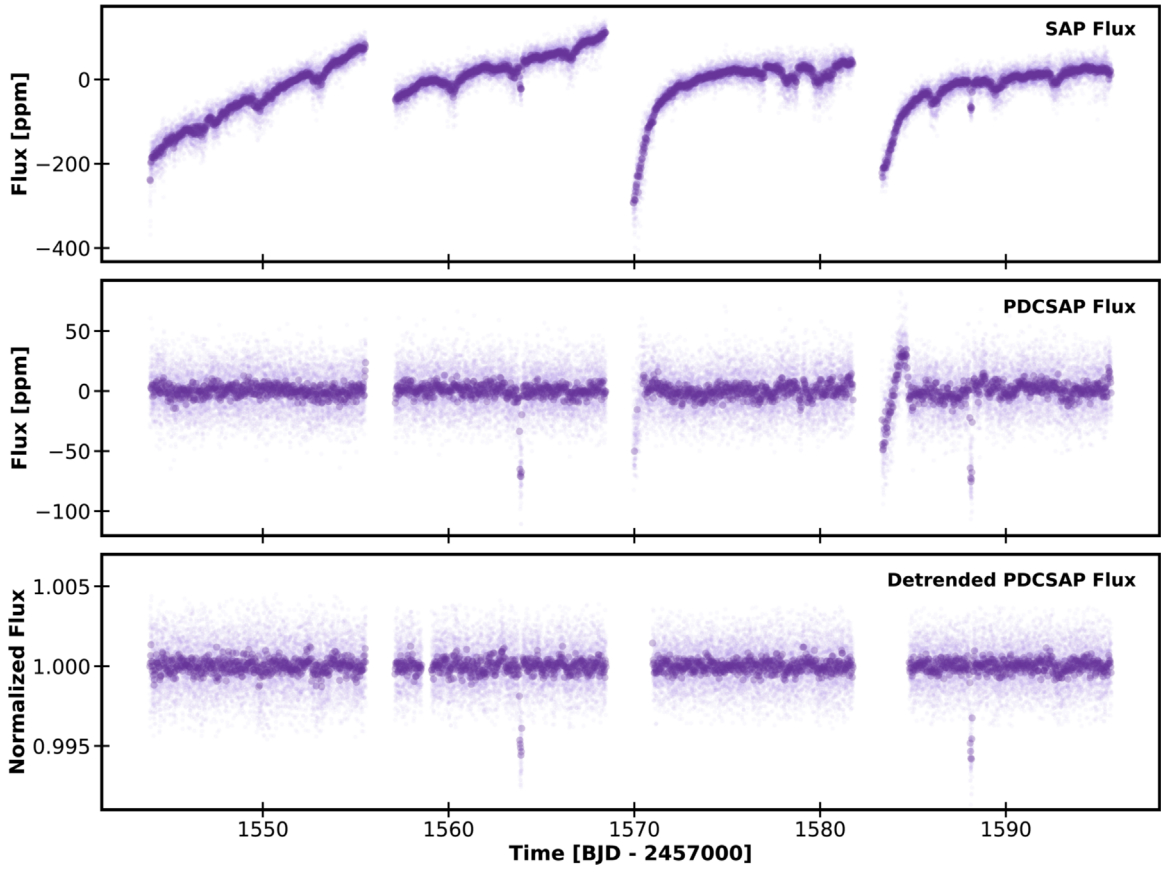


**Figure 2.** TESS light curves: simple aperture photometry (*SAP, top*), presearch data conditioned SAP (*PDCSAP, middle*), and orbit-by-orbit detrended PDCSAP (*bottom*). Lighter points depict the TESS 2-minute cadence flux measurements; darker points are the same data binned into 30-minute intervals. The two transit events can be clearly seen as brief flux dips in the middle and bottom panels.

#### 3.2.2. ASTEP 0.4 m Observations

We observed two full transits of TOI-1231 with the Antarctica Search for Transiting ExoPlanets (ASTEP) program on the East Antarctic plateau (Guillot et al. 2015; Mékarnia et al. 2016). The 0.4 m telescope is equipped with an FLI Proline science camera with a KAF-16801E, $4096 \times 4096$ front-illuminated CCD. The camera has an image scale of $0\farcs93$ pixel$^{-1}$, resulting in a $1^\circ \times 1^\circ$ corrected field of view. The focal instrument dichroic plate splits the beam into a blue wavelength channel for guiding, and a nonfiltered red science channel roughly matching an $R_c$ transmission curve. The telescope is automated or remotely operated when needed. Due to the extremely low data transmission rate at the Concordia Station, the data are processed on-site using an automated IDL-based pipeline, and the result is reported via email and then transferred to Europe on a server in Rome, Italy. The raw light curves of about 1000 stars are then available for deeper analysis. These data files contain each star's flux computed through various fixed circular apertures' radii, so that optimal light curves can be extracted (Figure 5, third panel). For TOI-1231, an 11 pixels ($10\farcs3$) radius aperture was found to give the best results.

The observations took place on UTC 2020 May 6 and August 11. Weather was good to acceptable, and air temperatures ranged between $-50\,^\circ$C and $-70\,^\circ$C. Two full transits, including the ingress and egress, were detected. Two other transits of TOI-1231 b were also detected on May 30 and June 26, but were partial or affected by technical issues, and are generally of lower signal-to-noise, and are thus not included in the present analysis. In each case, the ingress and egress occurred at the predicted times (with an uncertainty of a few minutes or less), indicating that any transit time variation must be small.

#### 3.2.3. ExTrA 0.6 m Observations

The ExTrA facility (Bonfils et al. 2015), located at La Silla observatory, consists of a near-infrared (0.85–1.55 $\mu$m) multi-object spectrograph fed by three 60 cm telescopes. At the focal plane of each telescope, 5 fiber positioners pick the light from the target and 4 comparison stars. We observed 2 full transits of TOI-1231 b on UTC 2020 March 18 and 2021 January 27 (Figure 3). The first night we observed with 3 telescopes using the fibers with $8''$ apertures. The second night we observed with 2 telescopes and $4''$ aperture fibers. Both nights we used the high-resolution mode of the spectrograph ($R \sim 200$) and 60 s exposures. We also observed 2MASS J10283882-5234151, 2MASS J10285562-5220140, 2MASS J10273532-5206553, and 2MASS J10271569-5239330, with J magnitude (Skrutskie et al. 2006) and $T_{\rm eff}$ (Gaia Collaboration et al. 2018) similar to TOI-1231, for use as comparison stars. The resulting ExTrA data were analyzed using custom data reduction software.

The ExTrA light curves are affected by systematic effects that are currently under investigation. To account for them, we modeled the transits observed by ExTrA with `juliet` (Kreidberg 2015; Espinoza et al. 2019; Speagle 2020), and included the quasi-periodic kernel Gaussian process implemented in `celerite`

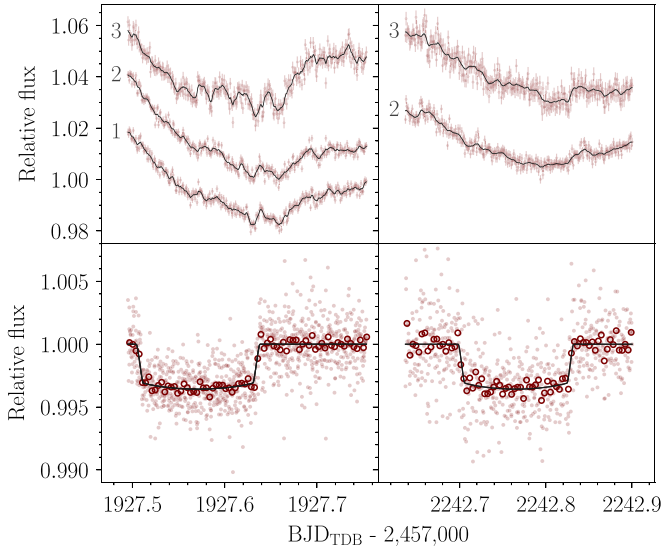


**Figure 3.** Light curves obtained by the ExTrA facility on nights UTC 2020 March 18 (*left*) and 2021 January 27 (*right*). Top panels show the Raw ExTrA photometry of each telescope (*labeled 1, 2, and 3*), displaced vertically for clarity, and a black curve depicting the median of the posterior of the modeling. Bottom panels show the light curves after correction with the maximum a posteriori model, with individual observations as light points, 5-minute bins as dark circles, and the maximum a posteriori transit model as a black line.

(Foreman-Mackey et al. 2017), with different kernel hyperparameters for each ExTrA telescope and for each night. We used a prior for the stellar density of $\rho_\star = 6.48 \pm 0.30\,\mathrm{g\,cm^{-3}}$ (Stassun et al. 2019), and non-informative priors for the rest of the parameters. The posterior provides the timings of the observed transits: $2458927.5716 \pm 0.0013\,\mathrm{BJD_{TDB}}$, and $2459242.7657 \pm 0.0013\,\mathrm{BJD_{TDB}}$, a planet to star radius ratio of $R_P/R_* = 0.0660^{+0.0072}_{-0.0086}$, and an impact parameter of $b = 0.201^{+0.091}_{-0.12}$. These transit light curves are not used in the global EXOFATv2 fit described in Section 4 in order to avoid biasing the final results due to the systematics present in the ExTrA data. However, the timing of the second transit is used as a prior for the time of conjunction ($T_C$) to better constrain the period of the planet.

### 3.3. Time Series Radial Velocities

Shortly after the discovery of the planet candidate by the TSTPC WG, we began radial velocity (RV) follow-up efforts using the Planet Finder Spectrograph (PFS) on Las Campanas Observatory's 6.5 m Magellan Clay telescope (Crane et al. 2006, 2008, 2010). PFS is an iodine cell-based precision RV spectrograph with an average resolution of $R \simeq 130{,}000$. RV values are measured by placing a cell of gaseous $I_2$, which has been scanned at a resolution of 1 million using the National Institute of Standards and Technology Fourier transform spectrometer (Nave 2017), in the converging beam of the telescope. This cell imprints the 5000–6200 Å region of the incoming stellar spectra with a dense forest of $I_2$ lines that act as a wavelength calibrator and provide a proxy for the point-spread function (PSF) of the spectrometer (Marcy & Butler 1992).

The spectra are split into 2 Å chunks, each of which is analyzed using the spectral synthesis technique described in Butler et al. (1996), which deconvolves the stellar spectrum from the $I_2$ absorption lines and produces an independent measure of the wavelength, instrument PSF, and Doppler shift. The final Doppler velocity from a given observation is the weighted mean of the velocities of all the individual chunks (~800 for PFS). The final internal uncertainty of each velocity is the standard deviation of all 800 chunk velocities about that mean.

**Table 2**
Binned RV data of TOI-1231

| Date [BJD$_{TDB}$] | RV [m s$^{-1}$] | $\sigma_{RV}$ [m s$^{-1}$] |
|---|---|---|
| 2458618.501473 | −10.13 | 1.19 |
| 2458625.551234 | 0.32 | 1.44 |
| 2458627.574495 | 3.73 | 1.17 |
| 2458677.491563 | 7.16 | 1.27 |
| 2458679.483330 | 5.96 | 1.22 |
| 2458685.500395 | 2.12 | 1.44 |
| 2458827.826089 | 3.29 | 1.06 |
| 2458828.842260 | −0.34 | 1.08 |
| 2458833.804469 | −9.11 | 1.27 |
| 2458836.814827 | −4.43 | 1.01 |
| 2458883.799738 | −4.85 | 1.21 |
| 2458885.807135 | −0.57 | 1.24 |
| 2458886.798816 | −2.90 | 1.31 |
| 2458890.781648 | 1.10 | 1.17 |

A total of 28 PFS radial observations were obtained from 2019 May to 2020 February, binned into 14 velocity measurements, with a mean internal uncertainty of 1.22 m s$^{-1}$(Table 2). A generalized Lomb–Scargle (GLS) periodogram of the PFS RV data shows a significant peak at 24 days (Figure 4), which matches the orbital period determined from the TESS data.

## 4. System Parameters from EXOFASTv2

To fully characterize the TOI-1231 system, we used the EXOFASTv2 software package (Eastman et al. 2013, 2019) to perform a simultaneous fit to the star's broadband photometry, the TESS, LCO, and ASTEP time series photometry, and the PFS radial velocity measurements. We applied Gaussian priors to the parallax and $V$-band extinction of the star using the results of Gaia EDR3 ($\varpi = 36.3726 \pm 0.0163$, corrected using the Lindegren et al. 2021 prescription) and Lallement et al. (2018) ($A_v = 0.003 \pm 0.0465$), respectively. Gaussion priors were also placed on the TOI-1231's mass ($M_\star$=0.461 ± 0.018 $M_\odot$, calculated using the prescription in Mann et al. 2019), effective temperature ($T_{\rm eff} = 3562 \pm 101$ K, taken from Gaidos et al. 2014), and metallicity ([Fe/H] = 0.05 ± 0.08 (see Section 2.5 for details). We disabled EXOFASTv2's MIST isochrone fitting option, which is less reliable for low-mass stars (Eastman et al. 2019). Finally, we placed a prior on the planet's time of conjunction derived from the ExTrA photometry (3.2.3). We did not place any constraints on the planet's period or orbital eccentricity.

EXOFASTv2's SED fitting methodology differs from the approach used in the SED-only fit that helped verify TOI-1231's suitability for precision radial-velocity follow up in Section 2.3. In place of the NextGen atmospheric models, EXOFASTv2 instead uses pre-computed bolometric corrections in a grid of $\log g$, $T_{\rm eff}$, [Fe/H], and $V$-band extinction.[61] This grid is based on the ATLAS/SYNTHE stellar atmospheres (Kurucz 2005) and the detailed shapes of the broadband photometric filters.

[61] http://waps.cfa.harvard.edu/MIST/model_grids.html#bolometric

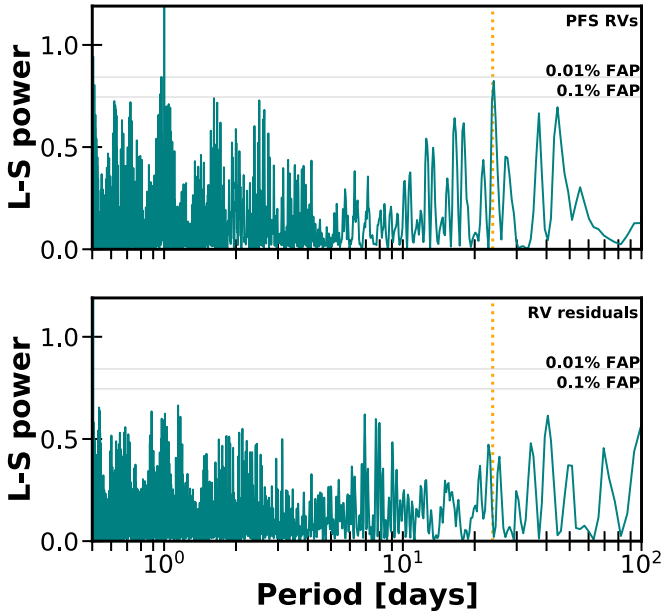


**Figure 4.** *Top*: Generalized Lomb–Scargle periodogram of the radial velocity measurements from PFS. There is a clear peak at period of TOI-1231 b (orange dotted line). *Bottom*: GLS of the radial velocity residuals, after the signal for planet b has been removed. No significant peaks remain in the data to suggest the presence of additional planets and/or stellar rotational signals.

We note that neither the raw TESS time series photometry nor the PFS RV measurements exhibit the type of sinusoidal variations that we would expect to see if the star were subject to rotation-based activity due to active regions such as star spots or plages crossing the visible hemisphere (Saar & Donahue 1997; Robertson et al. 2020). This lack of rotational modulation suggests an inactive star, a claim further supported by the lack of emission or any detectable temporal changes in the core of the H-$\alpha$ line (see, e.g., Reiners et al. 2012; Robertson et al. 2013). We therefore do not include any additional activity-based terms or detrending efforts when fitting either the photometric or radial velocity data.

The median EXOFASTv2 parameters for the TOI-1231 system are shown in Table 3, and the best fits to the TESS, LCO, and ASTEP photometry and the PFS radial velocity data are shown in Figure 5. The scatter in a star's radial velocity measurements includes any unmodeled instrumental effects or stellar variability. To address this, we include a "jitter" term in the RV fit, which is used to encompass uncorrelated signals in the star's own variability or PFS's systematics that occur on timescales shorter than the observational baseline. This value is added in quadrature to the internal uncertainties reported in the PFS data set to produce the RV error bars seen in Figure 5. The best-fit orbital eccentricity ($e = 0.087^{+0.012}_{-0.061}$) should not be regarded as statistically significant as it does not meet the criteria of being at least $2.45\sigma$ from 0, which is necessary to avoid falling subject to the Lucy–Sweeney bias (Lucy & Sweeney 1971). Even though the best-fit eccentricity is consistent with a circular orbit, we do not enforce a zero eccentricity fit because even a small amount of non-modeled eccentricity can bias the resulting orbital parameters and underestimate the uncertainties in many covariant parameters.

The mass of TOI-1231 b is measured to be $15.5 \pm 3.3\,M_\oplus$, which, when combined with the measured planet radius of $3.65^{+0.16}_{-0.15}\,R_\oplus$, results in a bulk density of $1.74^{+0.47}_{-0.42}$ g cm$^{-3}$, making the planet slightly denser than Neptune ($\rho_{\rm Nep} = 1.638$g m$^{-3}$).

## 5. Discussion

Barclay et al. (2018) predict that TESS will find just one non-rocky Neptune-sized or smaller planet in the habitable zone of an M dwarf brighter than $J = 10$. While the final number may be slightly higher, TOI-1231 b is the first confirmed TESS planet to meet these criteria. One method for comparing planets' potential for atmospheric characterization via transmission spectroscopy is the transmission spectroscopy metric (TSM, Kempton et al. 2018). A planet's TSM is proportional to its transmission spectroscopy signal-to-noise and is based on the strength of its expected spectral features (derived from its radius and scale height and the radius of the host star) and the host star's apparent $J$-band magnitude. With a TSM of $99 \pm 25$, TOI-1231 b planet ranks among the highest TSM Neptunes of any temperature in the pre-TESS era (Figure 6, Guo et al. 2020).

TOI-1231 b is one of the coolest planets accessible for atmospheric studies with $T_{\rm eq} = 330$ K.[62] Until recently it appeared that cooler planets had smaller spectral features, perhaps due to the increasing number of condensates that can form at lower temperatures (Crossfield & Kreidberg 2017). However, new observations of water features in the habitable-zone planet K2-18 b break this trend (Tsiaras et al. 2019; Benneke et al. 2019b). The K2-18 b water feature is very intriguing: it is suggestive of a qualitative change in atmospheric properties near the habitable zone. Perhaps condensates rain out (analogous to the L/T transition in brown dwarfs), and/or photochemical haze production is less efficient (Saumon & Marley 2008; Morley et al. 2013). However, K2-18 b is the only planet below 350 K with a measured transmission spectrum. TOI-1231 b provides an intriguing addition to the atmospheric characterization sample in this temperature range to determine whether K2-18 b is representative or an outlier. Recently, four *Hubble Space Telescope* (*HST*) transit observations were awarded to measure the near-infrared transmission spectrum of TOI-1231 b with the Wide Field Camera 3 (WFC3) instrument (GO 16181; PI L. Kreidberg).

### 5.1. Simulated Atmospheric Retrievals

To estimate how well the atmospheric properties could be extracted with *HST*, we used the open-source `petitRADTRANS` package (Mollière et al. 2019) to derive transmission spectra of TOI-1231 b, based on a simple atmospheric model. The atmosphere probed by the observations was assumed to be isothermal, at the equilibrium temperature derived for the planet in this work. Next, equilibrium chemistry was used to calculate the absorber abundances in the atmosphere, obtained with the chemistry model that is part of `petitCODE` (Mollière et al. 2017). We assumed two different compositional setups, 3 and 100× solar (Jupiter and Neptune-like, respectively), at a solar C/O. In addition, we introduced a gray cloud deck and modeled its effect on the spectrum when placing it between 100 and $10^{-6}$ bar, in 1 dex steps. The model with the highest cloud

[62] We note that $T_{\rm eq}$ is calculated using Equation (1) of Hansen & Barman (2007), which assumes no albedo and perfect redistribution. As such the quoted statistical error is likely severely underestimated relative to the systemic errors inherent in this assumption.

**Table 3**
Median Values and 68% Confidence Interval for EXOFASTv2 Results on TOI-1231

| Parameter | Units | Values |
|---|---|---|
| EXOFASTv2 Gaussian Priors: | | |
| $M_*$..... | Stellar mass ($M_\odot$) ..... | $0.485 \pm 0.024$ |
| $T_{\rm eff}$..... | Effective Temperature (K) ..... | $3562 \pm 101$ |
| [Fe/H]..... | Metallicity (dex) ..... | $0.05 \pm 0.08$ |
| $\varpi$..... | Parallax (mas)..... | $36.3726 \pm 0.0163$ |
| $A_V$..... | $V$-band extinction (mag)..... | $0.0031 \pm 0.0465$ |
| Stellar Parameters: | | |
| $M_*$..... | Mass ($M_\odot$)..... | $0.485 \pm 0.024$ |
| $R_*$..... | Radius ($R_\odot$)..... | $0.476^{+0.015}_{-0.014}$ |
| $R_{*,\rm SED}$..... | Radius[a] ($R_\odot$)..... | $0.4766 \pm 0.0084$ |
| $L_*$..... | Luminosity ($L_\odot$)..... | $0.0326 \pm 0.0010$ |
| $F_{\rm Bol}$..... | Bolometric Flux ($10^{-9}$ erg s$^{-1}$ cm$^{-2}$)..... | $1.381^{+0.043}_{-0.044}$ |
| $\rho_*$..... | Density (g cm$^{-3}$)..... | $6.31^{+0.68}_{-0.64}$ |
| $\log g$..... | Surface gravity (log(cm s$^{-2}$)) | $4.767^{+0.033}_{-0.035}$ |
| $T_{\rm eff}$.... | Effective Temperature (K).... | $3553^{+51}_{-52}$ |
| $T_{\rm eff,SED}$.... | Effective Temperature[a] (K).... | $3553 \pm 31$ |
| [Fe/H].... | Metallicity (dex).... | $0.041^{+0.069}_{-0.063}$ |
| $A_V$.... | $V$-band extinction (mag).... | $0.030^{+0.033}_{-0.021}$ |
| $\sigma_{\rm SED}$.... | SED photometry error scaling .... | $2.09^{+0.52}_{-0.37}$ |
| $\varpi$.... | Parallax (mas).... | $36.373 \pm 0.016$ |
| $d$.... | Distance (pc).... | $27.493 \pm 0.012$ |
| Planetary Parameters: | | b |
| $P$.... | Period (days).... | $24.245586^{+0.000064}_{-0.000066}$ |
| $R_P$.... | Radius ( $R_{\rm E}$).... | $3.65^{+0.16}_{-0.15}$ |
| $M_P$.... | Mass ( $M_{\rm E}$).... | $15.4 \pm 3.3$ |
| $T_C$.... | Time of conjunction (BJD$_{TDB}$).... | $2458563.88838^{+0.00057}_{-0.00058}$ |
| $T_T$.... | Time of minimum projected separation (BJD$_{TDB}$).... | $2458563.88839^{+0.00057}_{-0.00058}$ |
| $T_0$.... | Optimal conjunction Time (BJD$_{TDB}$) | $2458685.11630^{+0.00048}_{-0.00049}$ |
| $a$ | Semimajor axis (au) | $0.1288^{+0.0021}_{-0.0022}$ |
| $i$ | Inclination (Degrees) | $89.73 \pm 0.18$ |
| $e$ | Eccentricity | $0.087^{+0.12}_{-0.061}$ |
| $\omega_*$ | Argument of Periastron (Degrees) | $176^{+81}_{-90}$ |
| $T_{\rm eq}$ | Equilibrium temperature (K) | $329.6^{+3.8}_{-3.7}$ |
| $\tau_{\rm circ}$ | Tidal circularization timescale (Gyr) | $20600^{+9500}_{-8600}$ |
| $K$ | RV semi-amplitude (m s$^{-1}$) | $5.6 \pm 1.2$ |
| $R_P/R_*$ | Radius of planet in stellar radii | $0.0701^{+0.0019}_{-0.0017}$ |
| $a/R_*$ | Semimajor axis in stellar radii | $58.1 \pm 2.0$ |
| $\delta$ | Transit depth (fraction) | $0.00492^{+0.00027}_{-0.00024}$ |
| *Depth* | Flux decrement at mid transit | $0.00492^{+0.00027}_{-0.00024}$ |
| $\tau$ | Ingress/egress transit duration (days) | $0.00946^{+0.0018}_{-0.00066}$ |
| $T_{14}$ | Total transit duration (days) | $0.1350^{+0.0017}_{-0.0014}$ |
| $T_{\rm FWHM}$ | FWHM transit duration (days). | $0.1251 \pm 0.0013$ |
| $b$. | Transit Impact parameter . | $0.27^{+0.19}_{-0.18}$ |
| $b_S$. | Eclipse impact parameter . | $0.27^{+0.14}_{-0.18}$ |
| $\tau_S$. | Ingress/egress eclipse duration (days). | $0.00961^{+0.00085}_{-0.00077}$ |
| $T_{S,14}$. | Total eclipse duration (days). | $0.136^{+0.012}_{-0.013}$ |
| $T_{S,\rm FWHM}$. | FWHM eclipse duration (days). | $0.126^{+0.012}_{-0.013}$ |
| $\delta_{S,2.5\mu m}$. | Blackbody eclipse depth at 2.5 $\mu$m (ppm). | $0.000522^{+0.00012}_{-0.000097}$ |
| $\delta_{S,5.0\ \mu m}$. | Blackbody eclipse depth at 5.0 $\mu$m (ppm). | $0.99^{+0.13}_{-0.11}$ |
| $\delta_{S,7.5\ \mu m}$. | Blackbody eclipse depth at 7.5 $\mu$m (ppm). | $10.49^{+1.0}_{-0.86}$ |
| $\rho_P$. | Density (g cm$^{-3}$). | $1.74^{+0.47}_{-0.42}$ |
| $logg_P$. | Surface gravity . | $3.054^{+0.094}_{-0.11}$ |
| $\Theta$. | Safronov Number | $0.079 \pm 0.017$ |
| $\langle F \rangle$ | Incident Flux ($10^9$ erg s$^{-1}$ cm$^{-2}$) | $0.00263^{+0.00013}_{-0.00014}$ |
| $T_P$ | Time of Periastron (BJD$_{TDB}$) | $2458543.7^{+4.8}_{-6.3}$ |
| $T_S$ | Time of eclipse (BJD$_{TDB}$) | $2458575.45^{+0.95}_{-2.3}$ |
| $T_A$ | Time of Ascending Node (BJD$_{TDB}$) | $2458557.57^{+0.57}_{-1.4}$ |
| $T_D$ | Time of Descending Node (BJD$_{TDB}$) | $2458569.62^{+0.63}_{-1.1}$ |
| $V_c/V_e$ | | $0.993^{+0.062}_{-0.048}$ |
| $e \cos \omega_*$ | | $-0.036^{+0.061}_{-0.15}$ |

**Table 3**
(Continued)

| Parameter | Units | Values | | |
|---|---|---|---|---|
| $e \sin \omega_*$ | | $0.002^{+0.046}_{-0.066}$ | | |
| $M_P \sin i$ | Minimum mass ( $M_E$) | $15.4 \pm 3.3$ | | |
| $M_P/M_*$ | Mass ratio | $0.000096^{+0.000021}_{-0.000020}$ | | |
| $d/R_*$ | Separation at mid transit | $57.5^{+4.3}_{-4.4}$ | | |
| $P_T$ | A priori non-grazing transit prob | $0.0162^{+0.0014}_{-0.0011}$ | | |
| $P_{T,G}$ | A priori transit prob | $0.0186^{+0.0016}_{-0.0013}$ | | |
| $P_S$ | A priori non-grazing eclipse prob | $0.01607^{+0.0016}_{-0.00069}$ | | |
| $P_{S,G}$ | A priori eclipse prob | $0.01849^{+0.0019}_{-0.00080}$ | | |
| Wavelength Parameters: | | R | z' | TESS |
| $u_1$ | linear limb-darkening coeff | $0.31^{+0.33}_{-0.22}$ | $0.20^{+0.25}_{-0.15}$ | $0.31 \pm 0.19$ |
| $u_2$ | quadratic limb-darkening coeff | $0.36^{+0.33}_{-0.44}$ | $0.22^{+0.34}_{-0.27}$ | $0.07^{+0.29}_{-0.23}$ |
| $A_D$ | Dilution from neighboring stars | ... | ... | $-0.001^{+0.046}_{-0.049}$ |
| Telescope Parameters: | | PFS velocities | | |
| $\gamma_{rel}$ | Relative RV Offset (m/s) | $0.11 \pm 0.91$ | | |
| $\sigma_J$ | RV Jitter (m/s) | $3.03^{+1.0}_{-0.72}$ | | |
| $\sigma_J^2$ | RV Jitter Variance .....[*****] | $9.2^{+7.2}_{-3.8}$ | | |

**Note.** Notes from Eastman et al. (2019): The optimal conjunction time ($T_0$) is the time of conjunction that minimizes the covariance with the planet's period and therefore has the smallest uncertainty. The equilibrium temperature of the planet ($T_{eq}$) is calculated using Equation (1) of Hansen & Barman (2007) and assumes no albedo and perfect heat redistribution. The tidal circularization timescale ($\tau_{circ}$) is calculated using Equation (3) from Adams & Laughlin (2006) and assumes $Q = 10^6$. The 3.6 $\mu$m and 4.6 $\mu$m secondary occultation depths use a blackbody approximation of the stellar flux, $F_\star$, at $T_{eff}$ and of the planetary flux, $F_p$, at $T_{eq}$ and are calculated using $\delta_{S,\lambda} = \frac{(R_p/R_\star)^2}{(R_p/R_\star)^2 + (F_\star/F_p)}$.

[a] This value ignores the systematic error and is for reference only.

pressure was assumed to be our cloud-free model, because the atmosphere will become optically thick at lower pressures. We included the gas opacities of the following line absorbers: $H_2O$, $CH_4$, CO, $CO_2$, Na, and K. In addition to the gray cloud, continuum opacity sources arising from $H_2$, He, CO, $H_2O$, $CH_4$, and $CO_2$ Rayleigh scattering, as well as $H_2$–$H_2$ and $H_2$–He collision-induced absorption, were included. We refer the reader to Mollière et al. (2019) for the references used for the opacities.

We generated mock observations for all cases described above and retrieved them with `petitRADTRANS`, using the `PyMultiNest` package (Buchner et al. 2014). The latter uses the nested sampling implementation `MultiNest` (Feroz et al. 2009). The synthetic *HST* WCF3 observations were created assuming a wavelength range of 1.12–1.65 $\mu$m, with 12 points spaced equidistantly in wavelength space. We estimated the uncertainties on the spectroscopic transit depths using the `Pandexo_HST` tool.[63] Assuming 4 *HST* transit observations, we expect uncertainties of 18 ppm on the transit in each spectral channel. This corresponds to ~0.6 times the transit signal of the planet's scale height, when assuming a 100× solar composition. For these retrievals we placed special emphasis on the detectability of $H_2O$ and $CH_4$, for which we implemented the method described in Benneke & Seager (2013): the abundances of all metal absorbers were retrieved freely, assuming vertically constant abundance profiles. The abundance of $H_2$ and He was found by requiring that the mass fractions of all species (metals + $H_2$ and He) add up to unity, with an abundance ratio of 3:1 between $H_2$ and He. Three retrievals were run for every synthetic observation: (i) nominal model, retrieving the abundances of all metal absorbers, as well as the cloud deck pressure; (ii) same as (i), but neglecting the $CH_4$ opacity and $CH_4$ abundance as a free parameter; (iii) same as (i), but neglecting the $H_2O$ opacity and $H_2O$ abundance as a free parameter.

For every synthetic observation we then derived three evidences for models (i), (ii), and (iii), using nested sampling retrievals. The Bayes factor $B$, which is the ratio of these evidences, then allows us to assess how strongly models including $CH_4$ or $H_2O$ are preferred (Bayes factor of models (i) and (ii) or models (i) and (iii), respectively). We used a boundary value of $B > 3$ to express strong preference for a given model, following Kass & Raftery (1995).

We show the synthetic *HST* observation of the clear, 100× solar case in Figure 7. Because the 100× solar case has a larger mean molecular weight, it is the more challenging of the two enrichment cases. In addition to the synthetic observation, the 16–18 and 2–98 percentile envelopes of the retrieved transit depth distribution are shown for the retrievals with models (i), (ii), and (iii), that is, the full model and the model neglecting the $CH_4$ or $H_2O$ opacity, respectively.

For these cases, we find very strong preference for including $CH_4$ in the model ($B = 10^8$) and no preference for including $H_2O$ ($H_2O$ and $CH_4$ have roughly equal abundances in the input model, but the CH4 opacity is larger than the $H_2O$ opacity at all wavelengths). Clouds are a possibility for such planets (Crossfield & Kreidberg 2017) and we find that from $P_{cloud} < 1$ mbar on it becomes challenging to detect atmospheric features at all, and the 3 models (i), (ii), and (iii) become indistinguishable. In summary, we conclude that TOI-1231 b is an excellent target for atmospheric characterization. With a few transit observations, it will be possible to detect spectral features in an atmosphere similar to that of K2-18 b (Benneke et al. 2019b; Tsiaras et al. 2019), enabling the first comparative planetology in the temperature range 250–350 Kelvin.

[63] https://exoctk.stsci.edu/

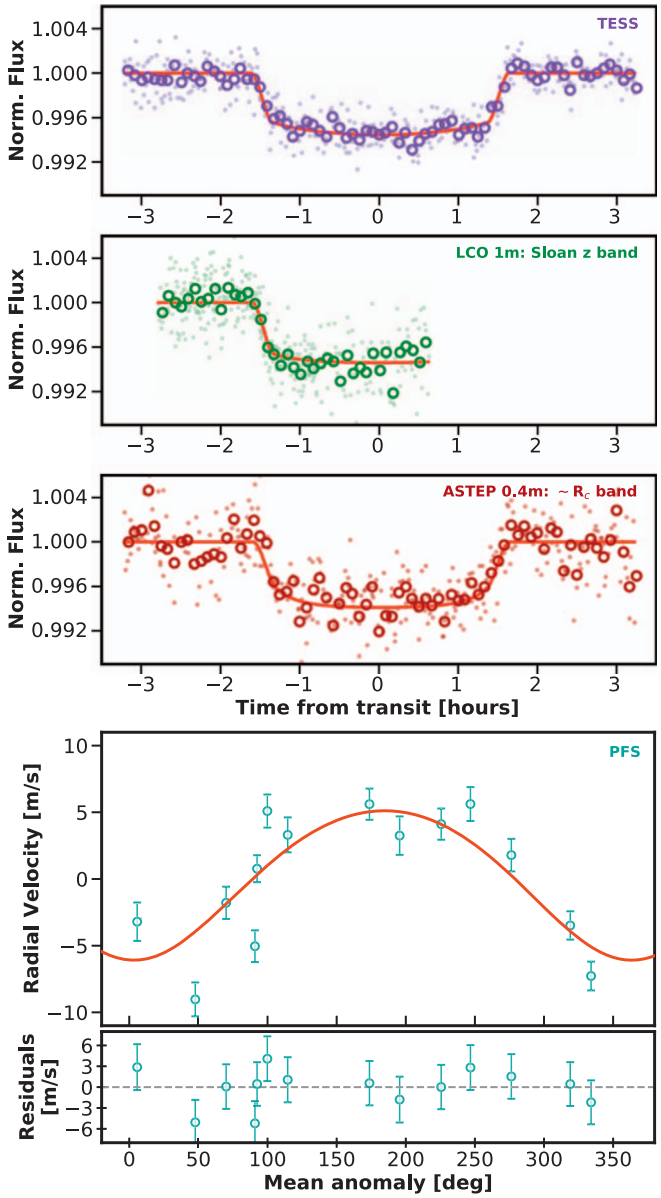


**Figure 5.** Results of the EXOFASTv2 joint fit to the TESS photometry, ground-based LCO and ASTEP, and PFS radial velocities. The top three panels show the phase-folded photometry data from TESS (2 full transits), LCO (2 partial transits), and ASTEP (2 full transits). All 3 photometry panels depict the unbinned data as light points, the 5-minute binned data as dark circles, and the best-fit model as a solid red line. The bottom panel shows the phase-folded RV measurements from PFS in cyan and the best-fit model in red. The RV residuals after the best-fit model has been subtracted from the data are displayed underneath the fit. Error bars in both RV panels are the quadrature sum of the PFS internal uncertainties and the RV jitter estimate from the EXOFASTv2 fit.

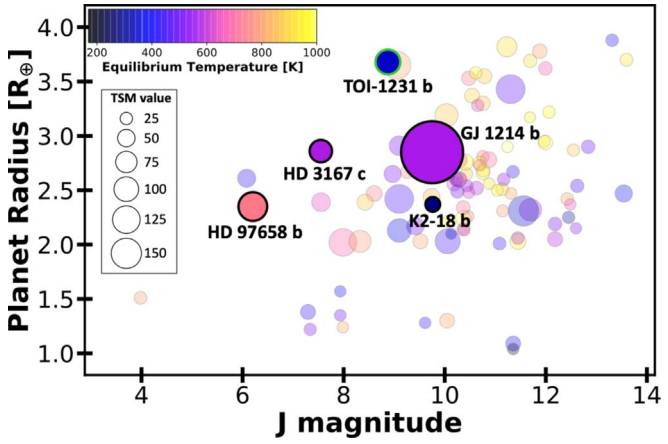


**Figure 6.** Transmission spectroscopy metric (TSM) values for small planets with $T_{eq} < 1000$ K compared with their radii and host star's J magnitude; data are taken from Guo et al. (2020). The 4 planets that have already had their atmospheres characterized by the *HST* are shown as solid circles and labeled. TOI-1231 b (green outline) offers another promising target in the cool, small planet regime and would, for the first time, enable comparisons in the $T_{eq} = 250$–$350$ K range when contrasted with K2-18 b.

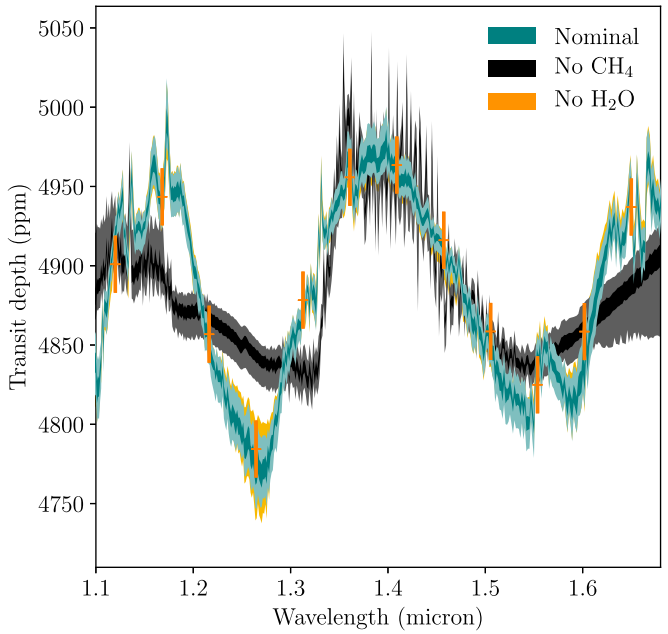


**Figure 7.** Synthetic *HST* observations and retrieval of the clear, 100× solar enrichment case. The 16–18 and 2–98 percentile envelopes of the retrieved flux distribution are shown for the retrievals with the full model (green envelopes) and the model neglecting $CH_4$ or $H_2O$ (black or orange envelopes, respectively).

### 5.2. *Prospects for* James Webb Space Telescope *(JWST) Observations*

With just 1 transit observed with *JWST*'s Near Infrared Imager and Slitless Spectrograph (NIRISS), for a clear, solar composition atmosphere, we expect to detect TOI-1231 b's spectrum (dominated by water at NIRISS wavelengths) with 90$\sigma$ significance (Kempton et al. 2018).

We also investigate prospects for a cloudy atmosphere, using PLATON (Zhang et al. 2019) to generate a solar composition model spectrum with a cloud deck pressure of 10 mbar (similar to GJ 3470b; Benneke et al. 2019a). We then used PandEXO (Batalha et al. 2017) to simulate a transmission spectrum for such an atmosphere. We find that even in this scenario, 1 transit with the NIRISS instrument would be sufficient to detect water absorption with 7.5$\sigma$ significance. For reference, this is 2$\sigma$ higher than the detection significance obtained with *6 HST* WFC3 transits for GJ 3470b (Benneke et al. 2019a), a planet with a similar size but much lower density (and also orbiting a 0.5 $R_\odot$ star).

### 5.3. *Probing Atmospheric Escape*

Given TOI-1231 b's low gravitational potential and expected X-ray and ultraviolet (XUV) instellation, we consider the likelihood that atmospheric escape is occurring and traceable

with H I Lyman $\alpha$ (Ly$\alpha$; 1216 Å) and the meta-stable He I line (10830 Å). TOI-1231 b's bulk density is similar to that of GJ 436 b ($1.80 \pm 0.29$ g m$^{-3}$; Maciejewski et al. 2014), a planet well known for its vigorously escaping atmosphere (Kulow et al. 2014; Ehrenreich et al. 2015). TOI-1231's fundamental stellar properties are very similar to GJ 436's, and our PFS spectra indicate that TOI-1231's $\log_{10} R'_{\rm HK} = -5.06$ is nearly equivalent to GJ 436's ($-5.09$; Boro Saikia et al. 2018), indicating the same level of magnetic activity. Because $R'_{\rm HK}$ is known to correlate well with UV emission (Youngblood et al. 2017), we assume GJ 436's synthetic X-ray and UV spectrum from Peacock et al. (2019) as a proxy for TOI-1231's. The integrated flux from 100 to 912 Å at 0.13 au is 172 erg cm$^{-2}$ s$^{-1}$ but could be as low as ~53 erg cm$^{-2}$ s$^{-1}$, according to the estimates from the MUSCLES Treasury Survey (France et al. 2016; Loyd et al. 2016; Youngblood et al. 2016) based on Linsky et al. (2014). In the energy-limited approximation (Salz et al. 2016), the mass-loss rate scales inversely with the planet's bulk density and inversely with the square of the orbital distance. Thus, under this approximation we expect a mass-loss rate about 14 times lower for TOI-1231 b than for GJ 436 b.

To better understand the properties of the escaping atmosphere of TOI-1231 b, we constructed a 1D model of this planet's upper atmosphere that solves the hydrodynamics equations for an escaping atmosphere and considers photochemistry at pressures $\lesssim$1 $\mu$bar, and radial distances from the planet center $r/R_P = 1$–10. We assume that the planet's bulk composition is dominated by $H_2$ and He, and set volume mixing ratios at the 1 $\mu$bar boundary of 0.9 for $H_2$ and 0.1 for He. The model is one-dimensional and spherically symmetric, appropriate to the substellar line. See García Muñoz et al. (2020) and references within for more details about the method. The model simulations shown in Figure 8 are specific to the stellar spectrum from Peacock et al. (2019) and assume supersonic conditions at $r/R_p \sim 10$. We take the stellar spectrum in its original format,[64] correcting only for orbital distance. A one-dimensional approach is expected to give a good representation of the flow within a few planetary radii from the surface, but cannot capture the shape of the flow after its interaction with the stellar wind. In any case, our predictions provide helpful insight to understand the prevalent forms of hydrogen, and the range of temperatures and velocities expected in the vicinity of the planet.

Figure 8 shows that $H_2$ remains abundant up to very high altitudes, and that the transition from H to $H^+$ also occurs at high altitude, a condition favorable for Ly$\alpha$ transit spectroscopy. Unlike for typical hot Jupiters, $H_3^+$ remains relatively abundant over an extended column and contributes to cooling of the atmosphere and to reducing the mass-loss rate. The model predicts that the planet is losing $2.3 \times 10^9$ g s$^{-1}$ (integrated over a solid angle $4\pi$).

We use the H I profile predicted by the model to estimate the Ly$\alpha$ transit depth attributable to hydrogen escaping the planet and before interacting with the stellar wind. This "cold" component is typically hidden by interstellar medium (ISM) absorption and has so far remained undetected. The Ly$\alpha$ absorption reported in other systems including GJ 436 b (e.g., Ehrenreich et al. 2015) is attributed to a "hot" component that results from charge exchange of the hydrogen atoms from the planet and the stellar wind protons (Khodachenko et al. 2019).

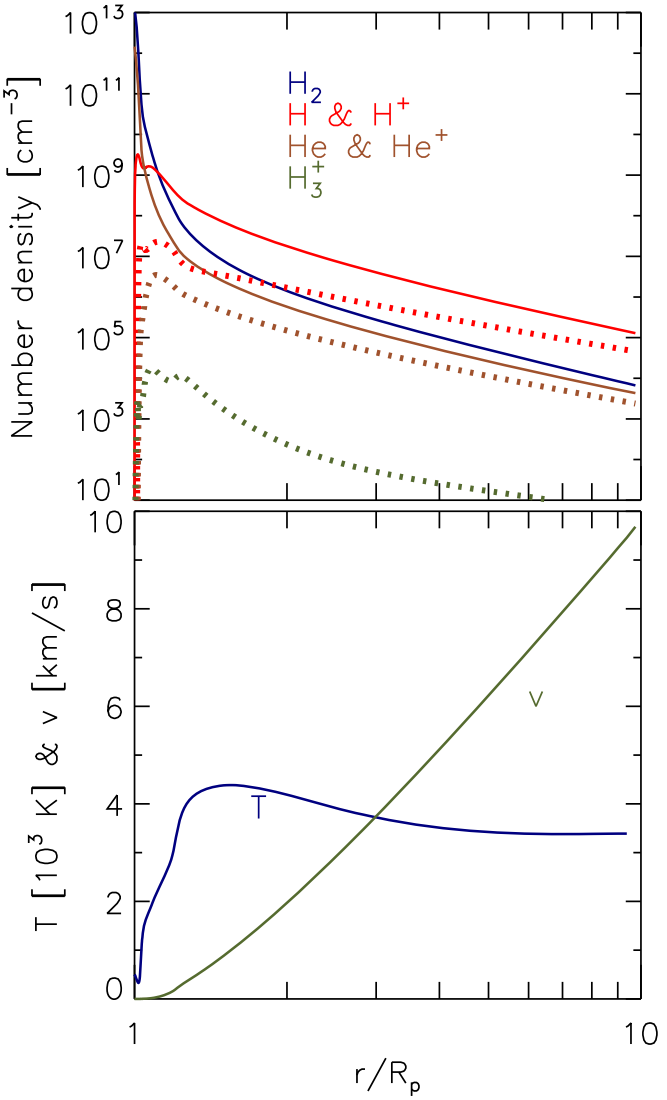


**Figure 8.** Results from the simulated upper atmosphere of TOI-1231 b. *Top panel:* the number density of $H_2$ (blue), H and $H^+$ (red), He and $He^+$ (brown), and $H_3^+$ (green) are shown as a function of distance ($r/R_p$) from the planet's 1-$\mu$m pressure level, which we approximate as the planet's optical radius ($R_p$). Neutrals are shown as solid lines and ions are shown as dotted lines. *Bottom panel:* The temperature ($10^3$ K; blue line) and outward bulk velocity (km s$^{-1}$; green line) are shown as a function of distance from the planet's 1-$\mu$m pressure level.

Despite the smaller expected escape rate with respect to other planets, TOI-1231 b's exosphere may be observable during a H I Ly$\alpha$ (1215.67 Å) transit. The host star's radial velocity (+70.5 km s$^{-1}$) Doppler shifts the entire system partially out of the bulk of ISM's H I attenuation region, allowing access to the core of the Ly$\alpha$ line and therefore to the "cold" component.

To assess the utility of a Ly$\alpha$ transit with *HST* for studying this planet, we estimate the profiles of the stellar Ly$\alpha$ emission, ISM attenuation, and planetary absorption (Figure 9). We use the reconstructed Ly$\alpha$ profile of GJ 436 (Youngblood et al. 2016) rescaled to match TOI-1231's distance. For the ISM, we assume a velocity centroid for the H I absorbers of $-4.3$ km s$^{-1}$ based on a kinematic model for the local ISM (Redfield & Linsky 2008) and a conservative H I column density $\log_{10}$

[64] http://archive.stsci.edu/hlsp/hazmat

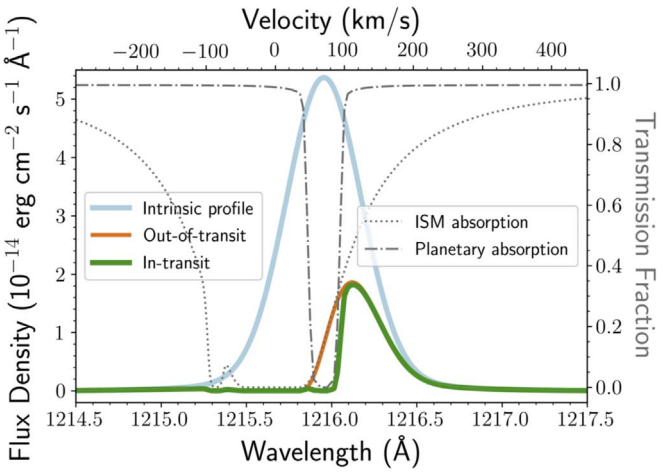


**Figure 9.** The flux densities of TOI-1231 at Earth without (blue) and with (orange) ISM attenuation and with ISM and in-transit planetary absorption (green). TOI-1231's intrinsic Ly$\alpha$ profile is scaled from GJ 436's and shifted to +70.5 km s$^{-1}$, and the ISM attenuation is conservatively assumed to be log N (HI) = 18.6, centered at −4 km s$^{-1}$(Redfield & Linsky 2008). The planetary absorption during transit is centered at 0 km s$^{-1}$ in the stellar rest frame. The dotted and dashed–dotted gray lines represent the ISM and in-transit planetary absorption, respectively (right axis). The transmission fraction ($e^{-\tau}$) is unity where all photons are transmitted and zero where all photons are absorbed.

N(HI) = 18.6 based on measured column densities of nearby sight lines (Wood et al. 2005; Youngblood et al. 2016; Waalkes et al. 2019). Using STScI's online exposure time calculator for STIS with the G140M, 1222 central wavelength, and $52'' \times 0\farcs2$ slit, we find that the expected planetary absorption around the Ly$\alpha$ line core (the "cold" component) could be detected at high confidence in a single transit.

We have not modeled the expected transit signature for meta-stable He I, but note the potential for exploring this planet's upper atmosphere with He I transits. However, as noted above, TOI-1231's XUV spectrum, which is responsible for both driving escape and populating the meta-stable He I state, is likely very similar to GJ 436's, and GJ 436 b's vigorously escaping atmosphere was not detected in He I (Nortmann et al. 2018). TOI-1231 b's larger orbit (a = 0.1266 au) further lowers its likelihood to be a promising He I target, as the farthest planet with a confirmed He I detection thus far is WASP 107 b, which has a semimajor axis of only 0.055 au and orbits a more favorable (to He I excitation) K6V star (Spake et al. 2018). See Oklopčić & Hirata (2018) and Oklopčić (2019) for more details on the prospects tracing atmospheric escape with meta-stable He I.

## 6. Conclusions

We reported the TESS discovery and confirmation (using several ground-based facilities) of TOI 1231 b, a temperate, Neptune-sized planet orbiting a nearby (27.6 pc) M dwarf star. The mass and radius of TOI-1231 b were measured to be $15.5 \pm 3.3\,M_\oplus$ and $3.65^{+0.16}_{-0.15}\,R_\oplus$, respectively. By virtue of its volatile, rich atmosphere; long transit duration; and small host star, TOI 1231 b appears to be one of the most promising small exoplanets for transmission spectroscopy with *HST* and *JWST* detected by the TESS mission thus far. It represents a rare and valuable addition to the current sample of just one other low-density Neptune-sized or smaller planet with an equilibrium temperature in the 250–350 K range and a transmission spectrum (K2-18 b). Moreover, its high systemic radial velocity makes it a particularly attractive target for atmospheric escape observations via the H I Lyman $\alpha$, and possibly the meta-stable He I line.

This planet also serves as excellent motivation for follow-up efforts focused on TESS single transit events (Villanueva et al. 2019), which is how TOI-1231 b would have presented itself if the host star was observed for only a single TESS sector.

This paper includes data collected by the TESS mission. Funding for the TESS mission is provided by NASA's Science Mission directorate. We acknowledge the use of public TESS alert data from pipelines at the TESS Science Office and the TESS Science Operations Center. This paper includes data gathered with the 6.5 meter Magellan Telescopes located at Las Campanas Observatory, Chile. This work makes use of observations from the LCOGT network and from the ASTEP telescope. ASTEP benefited from the support of the French and Italian polar agencies IPEV and PNRA in the framework of the Concordia Station program. This work has made use of data from the European Space Agency (ESA) mission Gaia (https://www.cosmos.esa.int/gaia), processed by the Gaia Data Processing and Analysis Consortium (DPAC, https://www.cosmos.esa.int/web/gaia/dpac/consortium). Funding for the DPAC has been provided by national institutions, in particular the institutions participating in the Gaia Multilateral Agreement. Some of the observations in the paper made use of the high-resolution-imaging instrument Zorro. Zorro was funded by the NASA Exoplanet Exploration Program and built at the NASA Ames Research Center by Steve B. Howell, Nic Scott, Elliott P. Horch, and Emmett Quigley. Zorro was mounted on the Gemini-South telescope of the international Gemini Observatory, a program of NSF's OIR Lab, which is managed by the Association of Universities for Research in Astronomy (AURA) under a cooperative agreement with the National Science Foundation on behalf of the Gemini partnership: the National Science Foundation (United States), National Research Council (Canada), Agencia Nacional de Investigación y Desarrollo (Chile), Ministerio de Ciencia, Tecnología e Innovación (Argentina), Ministério da Ciência, Tecnologia, Inovações e Comunicações (Brazil), and Korea Astronomy and Space Science Institute (Republic of Korea). Resources supporting this work were provided by the NASA High-End Computing (HEC) Program through the NASA Advanced Supercomputing (NAS) Division at Ames Research Center for the production of the SPOC data products. Some of the data presented in this paper were obtained from the Mikulski Archive for Space Telescopes (MAST). Support for MAST for non-*HST* data is provided by the NASA Office of Space Science via grant NNX13AC07G and by other grants and contracts. This research has made use of the NASA Exoplanet Archive, which is operated by the California Institute of Technology, under contract with the National Aeronautics and Space Administration under the Exoplanet Exploration Program. This research has made use of NASA's Astrophysics Data System. This research has also made use of the Exoplanet Follow-up Observation Program website, which is operated by the California Institute of Technology, under contract with the National Aeronautics and Space Administration under the Exoplanet Exploration Program. This research made use of Astropy, a community-developed core Python package for Astronomy (Astropy Collaboration et al. 2013). Part of this research was carried out at the Jet Propulsion

Laboratory, California Institute of Technology, under a contract with the National Aeronautics and Space Administration (NASA). D.D. acknowledges support from the TESS Guest Investigator Program grant 80NSSC19K1727 and NASA Exoplanet Research Program grant 18-2XRP18_2-0136. TD acknowledges support from MIT's Kavli Institute as a Kavli postdoctoral fellow. E.M. acknowledges support from NASA award 17-K2G06-0030. P.M. acknowledges support from the European Research Council under the European Union's Horizon 2020 research and innovation program under grant agreement No. 832428. T.G., A.A., L.A., D.M., F.-X.S. acknowledge support from Idex UCAJEDI (ANR-15-IDEX-01). D.J.S. acknowledges funding support from the Eberly Research Fellowship from The Pennsylvania State University Eberly College of Science. The Center for Exoplanets and Habitable Worlds is supported by the Pennsylvania State University, the Eberly College of Science, and the Pennsylvania Space Grant Consortium. This research received funding from the European Research Council (ERC) under the European Union's Horizon 2020 research and innovation program (grant agreement No. 803193/BEBOP), and from the Science and Technology Facilities Council (STFC; grant No. ST/S00193X/1). This publication makes use of VOSA, developed under the Spanish Virtual Observatory project supported by the Spanish MINECO through grant AyA2017-84089. VOSA has been partially updated by using funding from the European Union's Horizon 2020 Research and Innovation Programme, under grant agreement no 776403 (EXOPLANETS-A).

*Facilities:* TESS, Magellan: Clay (Planet Finder Spectrograph), Gemini-South (Zorro), SOAR, LCOGT, ASTEP.

*Software:* AstroImageJ (Collins et al. 2017), TAPIR (Jensen 2013), EXOFASTv2 (Eastman et al. 2019), petitCODE (Mollière et al. 2017), PyMultiNest (Buchner 2016), MultiNest (Feroz et al. 2009), Astropy (Astropy Collaboration et al. 2013).

## ORCID iDs

Jennifer A. Burt https://orcid.org/0000-0002-0040-6815
Diana Dragomir https://orcid.org/0000-0003-2313-467X
Allison Youngblood https://orcid.org/0000-0002-1176-3391
Antonio García Muñoz https://orcid.org/0000-0003-1756-4825
John McCann https://orcid.org/0000-0002-5155-6645
Laura Kreidberg https://orcid.org/0000-0003-0514-1147
Chelsea X. Huang https://orcid.org/0000-0003-0918-7484
Karen A. Collins https://orcid.org/0000-0001-6588-9574
Jason D. Eastman https://orcid.org/0000-0003-3773-5142
Carl Ziegler https://orcid.org/0000-0002-0619-7639
Joseph E. Rodriguez https://orcid.org/0000-0001-8812-0565
Eric E. Mamajek https://orcid.org/0000-0003-2008-1488
Keivan G. Stassun https://orcid.org/0000-0002-3481-9052
Samuel P. Halverson https://orcid.org/0000-0003-1312-9391
Steven Villanueva, Jr. https://orcid.org/0000-0001-6213-8804
R. Paul Butler https://orcid.org/0000-0003-1305-3761
Sharon Xuesong Wang https://orcid.org/0000-0002-6937-9034
Richard P. Schwarz https://orcid.org/0000-0001-8227-1020
George R. Ricker https://orcid.org/0000-0003-2058-6662
Roland Vanderspek https://orcid.org/0000-0001-6763-6562
David W. Latham https://orcid.org/0000-0001-9911-7388
S. Seager https://orcid.org/0000-0002-6892-6948
Joshua N. Winn https://orcid.org/0000-0002-4265-047X
Jon M. Jenkins https://orcid.org/0000-0002-4715-9460
Xavier Bonfils https://orcid.org/0000-0001-9003-8894
David Ciardi https://orcid.org/0000-0002-5741-3047
Jeffrey D. Crane https://orcid.org/0000-0002-5226-787X
Nicolas Crouzet https://orcid.org/0000-0001-7866-8738
Georgina Dransfield https://orcid.org/0000-0002-3937-630X
Fabo Feng https://orcid.org/0000-0001-6039-0555
Elise Furlan https://orcid.org/0000-0001-9800-6248
Tristan Guillot https://orcid.org/0000-0002-7188-8428
Arvind F. Gupta https://orcid.org/0000-0002-5463-9980
Steve B. Howell https://orcid.org/0000-0002-2532-2853
Eric L. N. Jensen https://orcid.org/0000-0002-4625-7333
Nicholas Law https://orcid.org/0000-0001-9380-6457
Andrew W. Mann https://orcid.org/0000-0003-3654-1602
Rachel A. Matson https://orcid.org/0000-0001-7233-7508
Djamel Mékarnia https://orcid.org/0000-0001-5000-7292
Joshua Pepper https://orcid.org/0000-0002-3827-8417
Nic Scott https://orcid.org/0000-0003-1038-9702
Stephen A. Shectman https://orcid.org/0000-0002-8681-6136
Joshua E. Schlieder https://orcid.org/0000-0001-5347-7062
François-Xavier Schmider https://orcid.org/0000-0003-3914-3546
Daniel J. Stevens https://orcid.org/0000-0002-5951-8328
Amaury H. M. J. Triaud https://orcid.org/0000-0002-5510-8751
David Charbonneau https://orcid.org/0000-0002-9003-484X
Zachory K. Berta-Thompson https://orcid.org/0000-0002-3321-4924
Christopher J. Burke https://orcid.org/0000-0002-7754-9486
Tansu Daylan https://orcid.org/0000-0002-6939-9211
Thomas Barclay https://orcid.org/0000-0001-7139-2724
Bill Wohler https://orcid.org/0000-0002-5402-9613
C. E. Brasseur https://orcid.org/0000-0002-9314-960X

## References

Adams, F. C., & Laughlin, G. 2006, ApJ, 649, 1004
Anders, F., Khalatyan, A., Chiappini, C., et al. 2019, A&A, 628, A94
Astropy Collaboration, Robitaille, T. P., Tollerud, E. J., et al. 2013, A&A, 558, A33
Barclay, T., Pepper, J., & Quintana, E. V. 2018, ApJS, 239, 2
Batalha, N. E., Lewis, T., Fortney, J. J., et al. 2019, ApJL, 885, L25
Batalha, N. E., Mandell, A., Pontoppidan, K., et al. 2017, PASP, 129, 064501
Bayo, A., Rodrigo, C., Barrado Y Navascués, D., et al. 2008, A&A, 492, 277
Benneke, B., Knutson, H. A., Lothringer, J., et al. 2019a, NatAs, 3, 813
Benneke, B., & Seager, S. 2013, ApJ, 778, 153
Benneke, B., Wong, I., Piaulet, C., et al. 2019b, ApJL, 887, L14
Bensby, T., Feltzing, S., & Oey, M. S. 2014, A&A, 562, A71
Bonfils, X., Almenara, J. M., Jocou, L., et al. 2015, Proc. SPIE, 9605, 96051L
Boro Saikia, S., Marvin, C. J., Jeffers, S. V., et al. 2018, A&A, 616, A108
Brown, T. M., Baliber, N., Bianco, F. B., et al. 2013, PASP, 125, 1031
Buchner, J. 2016, Stat. Comput., 26, 383
Buchner, J., Georgakakis, A., Nandra, K., et al. 2014, A&A, 564, A125
Burt, J. A., Nielsen, L. D., Quinn, S. N., et al. 2020, AJ, 160, 153
Butler, R. P., Marcy, G. W., Williams, E., et al. 1996, PASP, 108, 500
Cameron, A. C. 2012, Natur, 492, 48
Casagrande, L., Flynn, C., & Bessell, M. 2008, MNRAS, 389, 585

Collins, K. A., Kielkopf, J. F., Stassun, K. G., & Hessman, F. V. 2017, AJ, 153, 77
Crane, J. D., Shectman, S. A., & Butler, R. P. 2006, Proc. SPIE, 6269, 626931
Crane, J. D., Shectman, S. A., Butler, R. P., et al. 2010, Proc. SPIE, 7735, 773553
Crane, J. D., Shectman, S. A., Butler, R. P., Thompson, I. B., & Burley, G. S. 2008, Proc. SPIE, 7014, 701479
Crossfield, I. J. M., & Kreidberg, L. 2017, AJ, 154, 261
Cutri, R. M., Skrutskie, M. F., van Dyk, S., et al. 2003, yCat, II/246
Cutri, R. M., Wright, E. L., Conrow, T., et al. 2012, Explanatory Supplement to the WISE All-Sky Data Release Products
Dehnen, W. 2000, AJ, 119, 800
Dragomir, D., Teske, J., Günther, M. N., et al. 2019, ApJL, 875, L7
Eastman, J., Gaudi, B. S., & Agol, E. 2013, PASP, 125, 83
Eastman, J. D., Rodriguez, J. E., Agol, E., et al. 2019, arXiv:1907.09480
Ehrenreich, D., Bourrier, V., Wheatley, P. J., et al. 2015, Natur, 522, 459
ESA 1997, The Hipparcos and Tycho Catalogues, ESA SP-1200 (Noordwijk: ESA)
Espinoza, N., Kossakowski, D., & Brahm, R. 2019, MNRAS, 490, 2262
Feroz, F., Hobson, M. P., & Bridges, M. 2009, MNRAS, 398, 1601
Foreman-Mackey, D., Agol, E., Ambikasaran, S., & Angus, R. 2017, AJ, 154, 220
France, K., Loyd, R. O. P., Youngblood, A., et al. 2016, ApJ, 820, 89
Frith, J., Pinfield, D. J., Jones, H. R. A., et al. 2013, MNRAS, 435, 2161
Gagné, J., Mamajek, E. E., Malo, L., et al. 2018, ApJ, 856, 23
Gaia Collaboration, Brown, A. G. A., Vallenari, A., et al. 2018, A&A, 616, A1
Gaidos, E., Mann, A. W., Lépine, S., et al. 2014, MNRAS, 443, 2561
García Muñoz, A., Youngblood, A., Fossati, L., et al. 2020, ApJL, 888, L21
Guerrero, N. M., Seager, S., Huang, C. X., et al. 2021, ApJS, 254, 39
Guillot, T., Abe, L., Agabi, A., et al. 2015, AN, 336, 638
Guo, X., Crossfield, I. J. M., Dragomir, D., et al. 2020, AJ, 159, 239
Hansen, B. M. S., & Barman, T. 2007, ApJ, 671, 861
Henden, A. A., Templeton, M., Terrell, D., et al. 2016, yCat, II/336
Howell, S. B., Everett, M. E., Sherry, W., Horch, E., & Ciardi, D. R. 2011, AJ, 142, 19
Huang, C. X., Burt, J., Vanderburg, A., et al. 2018, ApJL, 868, L39
Jenkins, J. M., Twicken, J. D., McCauliff, S., et al. 2016, Proc. SPIE, 9913, 99133E
Jensen, E. 2013, Tapir: A web interface for transit/eclipse observability, Astrophysics Source Code Library, ascl:1306.007
Jiang, J. H., Ji, X., Cowan, N., Hu, R., & Zhu, Z. 2019, AJ, 158, 96
Johnson, J. A., & Apps, K. 2009, ApJ, 699, 933
Kass, R. E., & Raftery, A. E. 1995, Journal of the American Statistical Association, 90, 773
Kempton, E. M.-R., Bean, J. L., Louie, D. R., et al. 2018, PASP, 130, 114401
Khodachenko, M. L., Shaikhislamov, I. F., Lammer, H., et al. 2019, ApJ, 885, 67
Kirkpatrick, J. D., Schneider, A., Fajardo-Acosta, S., et al. 2014, ApJ, 783, 122
Kraus, A. L., & Hillenbrand, L. A. 2012, ApJ, 757, 141
Kreidberg, L. 2015, PASP, 127, 1161
Kulow, J. R., France, K., Linsky, J., & Parke Loyd, R. O. 2014, ApJ, 786, 132
Kurucz, R. L. 2005, MSAIS, 8, 14
Lallement, R., Capitanio, L., Ruiz-Dern, L., et al. 2018, A&A, 616, A132
Lépine, S., & Gaidos, E. 2011, AJ, 142, 138
Li, J., Tenenbaum, P., Twicken, J. D., et al. 2019, PASP, 131, 024506
Lindegren, L., Klioner, S. A., Hernández, J., et al. 2021, A&A, 649, A2
Linsky, J. L., Fontenla, J., & France, K. 2014, ApJ, 780, 61
Loyd, R. O. P., France, K., Youngblood, A., et al. 2016, ApJ, 824, 102
Lucy, L. B., & Sweeney, M. A. 1971, AJ, 76, 544
Luque, R., Pallé, E., Kossakowski, D., et al. 2019, A&A, 628, A39
Luyten, W. J. 1957, A Catalogue of 9867 Stars in the Southern Hemisphere, with Proper Motions Exceeding 0."2 Annually (Minneapolis, MN: Lund Press)
Luyten, W. J. 1979, New Luyten Catalogue of Stars with Proper Motions Larger than Two Tenths of an Arcsecond (Minneapolis, MN: Lund Press)
Maciejewski, G., Niedzielski, A., Nowak, G., et al. 2014, AcA, 64, 323
Mackereth, J. T., & Bovy, J. 2018, PASP, 130, 114501
Mamajek, E. E., Bartlett, J. L., Seifahrt, A., et al. 2013, AJ, 146, 154
Mann, A. W., Dupuy, T., Kraus, A. L., et al. 2019, ApJ, 871, 63
Mann, A. W., Feiden, G. A., Gaidos, E., Boyajian, T., & von Braun, K. 2015, ApJ, 804, 64
Marcy, G. W., & Butler, R. P. 1992, PASP, 104, 270
Mékarnia, D., Guillot, T., Rivet, J. P., et al. 2016, MNRAS, 463, 45
Mollière, P., van Boekel, R., Bouwman, J., et al. 2017, A&A, 600, A10
Mollière, P., Wardenier, J. P., van Boekel, R., et al. 2019, A&A, 627, A67
Monari, G., Famaey, B., Siebert, A., Wegg, C., & Gerhard, O. 2019, A&A, 626, A41
Morley, C. V., Fortney, J. J., Kempton, E. M. R., et al. 2013, ApJ, 775, 33
Morley, C. V., Marley, M. S., Fortney, J. J., et al. 2014, ApJ, 787, 78
Morris, R. L., Twicken, J. D., Smith, J. C., et al. 2017, Kepler Science Document KSCI-19081-002, 6
Muirhead, P. S., Dressing, C. D., Mann, A. W., et al. 2018, AJ, 155, 180
Nave, G. 2017, ESO Calibration Workshop: The Second Generation VLT Instruments and Friends (Santiago: ESO), 32
Nortmann, L., Pallé, E., Salz, M., et al. 2018, Sci, 362, 1388
Oklopčić, A. 2019, ApJ, 881, 133
Oklopčić, A., & Hirata, C. M. 2018, ApJL, 855, L11
Peacock, S., Barman, T., Shkolnik, E. L., et al. 2019, ApJ, 886, 77
Redfield, S., & Linsky, J. L. 2008, ApJ, 673, 283
Reiners, A., Joshi, N., & Goldman, B. 2012, AJ, 143, 93
Ricker, G. R., Winn, J. N., Vanderspek, R., et al. 2014, Proc. SPIE, 9143, 914320
Robertson, P., Endl, M., Cochran, W. D., & Dodson-Robinson, S. E. 2013, ApJ, 764, 3
Robertson, P., Stefansson, G., Mahadevan, S., et al. 2020, ApJ, 897, 125
Rodriguez, J. E., Quinn, S. N., Huang, C. X., et al. 2019, AJ, 157, 191
Saar, S. H., & Donahue, R. A. 1997, ApJ, 485, 319
Salz, M., Schneider, P. C., Czesla, S., & Schmitt, J. H. M. M. 2016, A&A, 585, L2
Saumon, D., & Marley, M. S. 2008, ApJ, 689, 1327
Schlaufman, K. C., & Laughlin, G. 2010, A&A, 519, A105
Schneider, A. C., Greco, J., Cushing, M. C., et al. 2016, ApJ, 817, 112
Schönrich, R., Binney, J., & Dehnen, W. 2010, MNRAS, 403, 1829
Skrutskie, M. F., Cutri, R. M., Stiening, R., et al. 2006, AJ, 131, 1163
Smith, J. C., Stumpe, M. C., Van Cleve, J. E., et al. 2012, PASP, 124, 1000
Spake, J. J., Sing, D. K., Evans, T. M., et al. 2018, Natur, 557, 68
Speagle, J. S. 2020, MNRAS, 493, 3132
Stassun, K. G., Collins, K. A., & Gaudi, B. S. 2017, AJ, 153, 136
Stassun, K. G., Corsaro, E., Pepper, J. A., & Gaudi, B. S. 2018, AJ, 155, 22
Stassun, K. G., Oelkers, R. J., Paegert, M., et al. 2019, AJ, 158, 138
Stassun, K. G., & Torres, G. 2016, AJ, 152, 180
Stumpe, M. C., Smith, J. C., Catanzarite, J. H., et al. 2014, PASP, 126, 100
Stumpe, M. C., Smith, J. C., Van Cleve, J. E., et al. 2012, PASP, 124, 985
Sullivan, P. W., Winn, J. N., Berta-Thompson, Z. K., et al. 2015, ApJ, 809, 77
Tokovinin, A., Mason, B. D., Hartkopf, W. I., Mendez, R. A., & Horch, E. P. 2018, AJ, 155, 235
Torres, S., Cai, M. X., Brown, A. G. A., & Portegies Zwart, S. 2019, A&A, 629, A139
Tsiaras, A., Waldmann, I. P., Tinetti, G., Tennyson, J., & Yurchenko, S. N. 2019, NatAs, 3, 1086
Twicken, J. D., Catanzarite, J. H., Clarke, B. D., et al. 2018, PASP, 130, 064502
Twicken, J. D., Clarke, B. D., Bryson, S. T., et al. 2010, Proc. SPIE, 7740, 774023
van Leeuwen, F., de Bruijne, J., Babusiaux, C., et al. 2021, Gaia EDR3 Documentation
Vanderspek, R., Huang, C. X., Vanderburg, A., et al. 2019, ApJL, 871, L24
Villanueva, S., Jr., Dragomir, D., & Gaudi, B. S. 2019, AJ, 157, 84
Waalkes, W. C., Berta-Thompson, Z., Bourrier, V., et al. 2019, AJ, 158, 50
Wang, S., Jones, M., Shporer, A., et al. 2019, AJ, 157, 51
Wood, B. E., Redfield, S., Linsky, J. L., Muller, H., & Zank, G. P. 2005, ApJS, 159, 118
Youngblood, A., France, K., Loyd, R., et al. 2016, ApJ, 824, 101
Youngblood, A., France, K., Loyd, R., et al. 2017, Astrophysical Journal, 843, 31
Zhang, M., Chachan, Y., Kempton, E. M. R., & Knutson, H. A. 2019, PASP, 131, 034501
Ziegler, C., Tokovinin, A., Briceño, C., et al. 2020, AJ, 159, 19